Ye, Z., Wang, L., Zhu, B., **Shao, H.**, Xu, W., Chen, Y. (2022):
A thermo-hydro-chemo-mechanical coupled model for natural gas hydrate-bearing sediments considering gravity effect
J. Nat. Gas Sci. Eng. **108** , art. 104823

A thermo-hydro-chemo-mechanical coupled model for natural gas hydrate-bearing sediments considering gravity effect

Zhigang Ye[1,4], Lujun Wang[2, *], Bin Zhu[3], Haibing Shao[4], Wenjie Xu[5], Yunmin Chen[6]

[1] MOE Key Laboratory of Soft Soils and Geoenvironmental Engineering, College of Civil Engineering and Architecture, Zhejiang University, Hangzhou, 310058, China. E-mail: zhigangye@zju.edu.cn.

[2, *] MOE Key Laboratory of Soft Soils and Geoenvironmental Engineering, Center for Hypergravity Experimental and Interdisciplinary Research, College of Civil Engineering and Architecture, Zhejiang University, Hangzhou, 310058, China. Corresponding author, E-mail: lujunwang@zju.edu.cn. ORCID: 0000-0002-0384-4941.

[3] MOE Key Laboratory of Soft Soils and Geoenvironmental Engineering, Center for Hypergravity Experimental and Interdisciplinary Research, College of Civil Engineering and Architecture, Zhejiang University, Hangzhou, 310058, China. E-mail: binzhu@zju.edu.cn.

[4] Department of Environmental Informatics, Helmholtz Centre for Environmental Research-UFZ, Permoserstr. 15, Leipzig, 04318, Germany. E-mail: haibing.shao@ufz.de.

[5] MOE Key Laboratory of Soft Soils and Geoenvironmental Engineering, College of Civil Engineering and Architecture, Zhejiang University, Hangzhou, 310058, China. E-mail: wenjiexu@zju.edu.cn.

[6] MOE Key Laboratory of Soft Soils and Geoenvironmental Engineering, College of Civil Engineering and Architecture, Zhejiang University, Hangzhou, 310058, China. E-mail: chenyunmin@zju.edu.cn.

Abstract: Natural gas hydrates have attracted many attentions recently as a promising energy, the exploitation of which will cause complicated multifield coupled behavior of hydrate-bearing sediments. As sediments usually vary from tens to hundreds of meters, the gravity effect on gas-liquid migration and soil deformation may not be completely ignored. This paper develops a new thermo-hydro-chemo-mechanical model to investigate the sediment behavior during the hydrate dissociation. The equations of gas-liquid migration are numerical solved with explicit incorporation of hydrate dissociation process. The numerical stability and efficiency have been improved by expanding the Taylor series of the source terms and making the first-order approximation. Furtherly, pre-calculation procedures have been considered to obtain the initial state of field variables. Pilot-scale model results show that the gas-liquid migration, soil deformation and NGH dissociation are accelerated when the gravity effect is present. During the exploitation, a dissociation front can be observed, and gas-liquid migration and hydrate dissociation dominate the process alternatively, leading to first decrease and subsequent increase of gas saturation and continuous rise of liquid saturation. Moreover, it is inferred that marginal enhancement of gas production can be achieved with the increase of wellbore lengths, but it should not exceed 75% of the reservoir thickness.

Keywords: natural gas hydrates; thermo-hydro-chemo-mechanical coupled; gravity effect; gas-liquid migration; hydrate dissociation; numerical modelling.

1 Introduction

The natural gas hydrates (NGHs) are caged crystalline compounds composed of natural gas and water molecules under high pressure and low temperature, and they are widely distributed in marine sediments and permafrost formations (Sloan and Koh, 2008). The amount of carbon stored in NGH reservoirs is estimated to be at least twice than that in traditional fossil fuels (Kvenvolden, 1988; Milkov, 2004). So far, several exploitation methods have been reported, including depressurization, heat stimulation and chemical injection (Yousif *et al*., 1991; Sun *et al*., 2014; Song *et al*., 2016). The NGH dissociation is an endothermic process, which absorbs heat from the surroundings, and then further affects soil stiffness and strength. Simultaneously, changes of pore pressures caused by released gas and liquid from NGHs will lead to variations of skeleton effective stresses, heat advection parameters and eventually the NGH dissociation itself. Besides, temperature change causes thermal expansions of all three phases in the sediments and the variation of NGH dissociation process, and skeleton deformation will reciprocally affect pore pressures.

These processes are recognized as the coupled thermo-hydro-chemo-mechanical (THCM) behavior during the NGH exploitation. Inappropriate depressurization rate or production wellbore layout may lead to abrupt variations and spatial inhomogeneity of effective stresses, thus possibly triggering geotechnical hazards, such as borehole collapse, seabed facility failures and submarine landslides (Maslin *et al*., 2010; McConnell *et al*., 2012). As the thickness of hydrate-bearing sediments varies from tens to hundreds of meters (Wang *et al*., 2017; Li *et al*., 2018; Ye *et al*., 2020), the pore gas / liquid pressure and skeleton effective stresses will vary alone the depth, resulting in altered fluid flow during the NGH exploitation (shown in Fig. 1). This may further enhance the spatial inhomogeneity of effective stresses and aforementioned hazards.

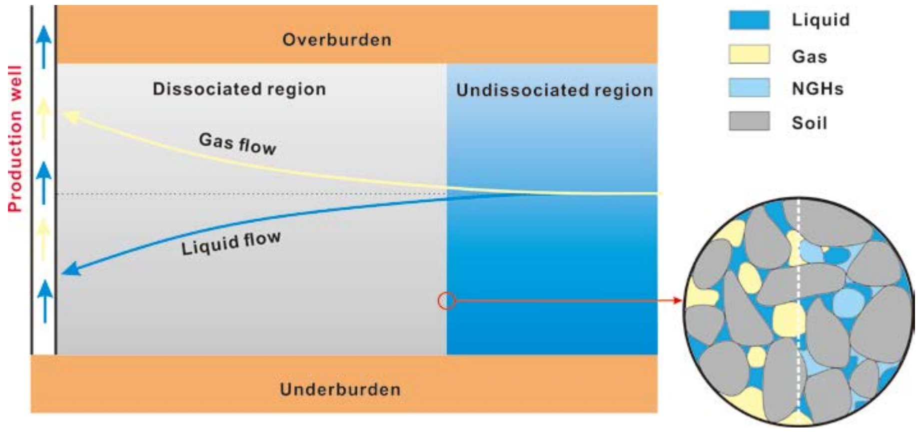

Fig. 1 Diagram of sediment phases and gravity effect on gas-liquid migration

So far, several countries have conducted in-situ NGH exploitation tests. The hydrate-bearing sediment in the Messoyakha field in Russia in the 1960s was the first report of such attempt (Makogon *et al*., 2007). In this field, gas in the hydrated state existed in the upper layer of the sediments and the underlying layer contained gas in a free state. In Mackenzie Delta of Northwest Territories in Canada, a longer in-situ hydrate exploitations were carried out in 2002, 2007 and 2008 (Yamamoto and Dallimore, 2008). Depressurization method was applied to the investigating study. This research program was believed to be a new step forward towards realizing NGHs as a viable energy resource. The Iġnik Sikumi field program on the Alaska North Slope in America in 2012 was designed to provide insight into the potential commercial gas production by adopting the CO_2-CH_4 swap process and extract nature gas from hydrate-bearing sediments (Boswell *et al*., 2017). With the application of depressurization method in Nankai Trough in Japan, the first successful oceanic NGH extraction was achieved in 2013 (Konno *et al*., 2017; Yu *et al*., 2019). During the test production, sand intrusion was detected and tests were terminated in 2013. Afterwards at site AT1-P in South China Sea, China, trial exploitations were carried out in 2017 and 2020 (Li *et al*., 2018; Ye *et al*., 2020), and daily gas production rate was recorded to be 0.51×10^4 m^3 and 2.87×10^4 m^3 for 60 and 30 days respectively, which holds the longest continuous extraction record so far. These in-situ exploitations are extremely valuable. For commercial operation, the gas production rate needs to reach at least 5.0×10^5 m^3/d in marine sediments (Sloan, 2003; Wang *et al*., 2022) and the production life of a particular site needs to be at least 10 years (Chen *et al*., 2022). According this standard, most of the NGH sites are still far from commercial production.

To comprehensively investigate the gas-liquid migration, hydrate-bearing sediment deformation and possible geotechnical hazards during the NGH dissociation, laboratory experiments and numerical simulations are often carried out and compared. Some laboratory-scale tests are conducted to analyze skeleton deformation (Miyazaki *et al*., 2011, 2012), porous fluid flow (Kleinberg *et al*., 2003; Kumar *et al*., 2010) and chemical reaction characteristics (Gayet *et al*., 2005; Chong *et al*., 2015), which greatly promote the basic understanding on the underlying mechanism for hydrate-bearing sediments. Taking Li's study (2014) for example, six experimental runs were carried out in a three-dimensional pressure vessel. Among them, four runs were used to calibrate the kinetic reactive parameters, where the relative deviations of gas pressure from the six experiments range from 2.9% to 10.5%. With the optimization (history-matching) process (Thomas *et al*., 1972; Moridis *et al*., 2005; Yin *et al*., 2018) providing estimates of the thermal properties and of the kinetic parameters, the minimized deviations between observations and simulation results have been found to be less than 3% (Moridis *et al*., 2005). Based on the scaling criteria, the parameters obtained in the laboratory can be up-scaled to reflect hydrate reservoir responses in the field (Bai *et al*., 2013; Kwon *et al*., 2013; Wang *et al*., 2014, 2016). Besides, initial pore pressures and stresses driven by gravity corresponding the prototypes play a critical role in these modeling cases.

As for numerical simulations, intensive THCM coupled models are performed with different codes, including Tough+Hydrate (Rutqvist *et al*., 2009; Jin *et al*., 2018b), Comsol (Sun *et al*., 2019), Code-bright (Sánchez *et al*., 2018). Wilder *et al*. (2008) and White *et al*. (2020) have made extensive reviews on the available numerical approaches simulating the hydrate behavior. The Tough+Hydrate code (Moridis *et al*., 2012) has been continually developed by Lawrence Berkeley National Laboratory (LBNL) to model non-isothermal CH_4 release with phase-change behavior, and is one of the mature simulators for hydrate dissociation. By simulating two known hydrate-bearing permafrost sediments with Tough+Hydrate+Flac, Rutqvist *et al* (2009) found that the depressurization-induced NGH dissociation increases shear stresses in dissociation regions and the Poisson’s ratio is a key parameter determining the effective stress path, possibly revealing the collapsed mechanism of boreholes. For the cross-platform finite element multi-physics code Comsol (COMSOL, 2017), user-friendly graphical user interface (GUI) and coupled systems of partial differential equations allows researchers to build and modify the model easily (Sun *et al*., 2018). Sun *et al* (2018) introduced a new thermodynamics-based constitutive model into Comsol with the external material interface and established a THCM coupled model for NGH exploitations, which is an effective method to reveal the complicated static and dynamic mechanical responses. Besides, gas production and ice thawing / formation in hydrate-bearing sediments considering dilatancy and anisotropy were simulated based on Code-bright (Sánchez *et al*., 2018), which is a finite element code originally developed by Olivella *et al* (1996) and designed to solve multiphase mass and heat transport problems. For simulating the complicated coupled processes during the NGH dissociation, computational efficiency is of great importance. In Code-bright, the mass balance for each component (i.e. water or air) combines the mass in all phases to eliminate the frequent change of source terms, and the accumulation terms are directly discretized by a finite difference in time, which reaches a more economical iteration (Olivella *et al*., 1996; Sánchez *et al*., 2018). In general, the numerical models are considered a valuable tool to predict the physical behavior of the reservoir before in-situ operations.

Gas / liquid pressure presents a gradient distribution along the depth by the gravity effect, thus making gas-liquid migration different from that neglecting it. To our best of knowledge, few researches were reported to analyze the gravity effect on NGH dissociation in detail. So, we wonder how much impact the gravity has on the THCM coupled behavior when NGH is exploited. Therefore, we comprehensively investigate the gravity effect based on a new developed THCM coupled model based on the open-source finite element code OpenGeoSys (OGS) (Kolditz *et al*., 2012; Lehmann *et al*., 2018; Bilke *et al*., 2019). To achieve a higher numerical stability and efficiency, mass change in source terms caused by NGH dissociation is expanded by Taylor series and explicitly solved locally. After verified against both experimental data and also previous numerical results, a pilot-scale model has been established to investigate the gravity effect. As the gas production rate is of great importance during the exploitation, it is important to know how much is the optimum length of vertical production wellbore in comparison to the reservoir thickness. Hence, the impacts of gravity effect on NGH dissociation and the influence of vertical wellbore length on gas production rate are investigated in detail using this numerical model. Conclusions are drawn in the end that will facilitate a more efficient exploitation of NGH resources.

2 Methodology

The THCM coupled responses of hydrate-bearing sediments mainly consist of NGH dissociation, skeleton deformation, gas / water migration and heat transfer. Fig. 2 illustrates their coupled relationship. In our numerical model, the following assumptions are adopted: (1) the solid, hydrate and liquid phases can thermally expand, whereas the gas thermal expansion is regulated by the Clapeyron's equation, (2) heat transfer includes conduction and advection, (3) Darcy's law and Fick's law are used to illustrate seepage and diffusion of pore water and dry air, with the phase-transition between liquid water and gaseous vapor also considered (Zhu *et al*., 2020), and (4) none of NGH secondary formation, ice formation and air dissolution happens during the NGH dissociation. Based on these assumptions, gas pressure p^{g}, liquid pressure p^{l}, temperature T and displacements $\mathbf{u}$ are treated as independent primary variables, leading to equations presented below.

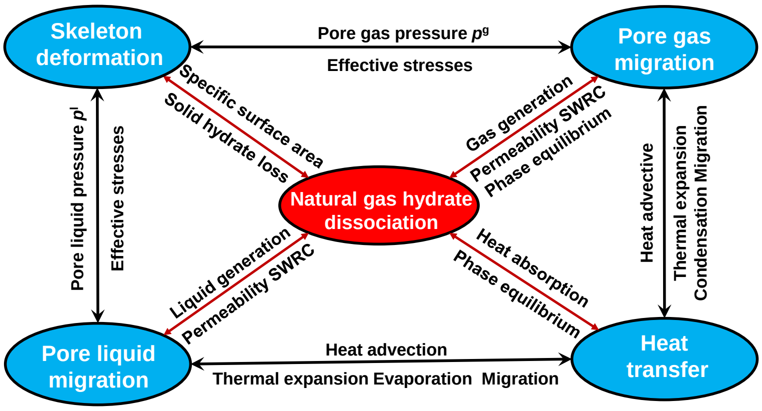

Fig. 2 Coupled processes of hydrate-bearing sediments during the NGH dissociation

2.1 Governing equations

2.1.1 Mass balance equations

The mass balance equations here are formulated for the air and water components. This means the water mass balance includes water in aqueous phase and also the water vapor in the gas phase, which can be formulated as (Wang *et al*., 2015):

$$\frac{\mathrm{d_s}}{\mathrm{d}t}\left(\rho_{\mathrm{a}}^{\mathrm{g}} S^{\mathrm{g}} \varphi\right)+\nabla\cdot(\mathbf{J}_{\mathrm{a}}^{\mathrm{g}})+\rho_{\mathrm{a}}^{\mathrm{g}} S^{\mathrm{g}} \varphi \nabla\cdot\frac{\mathrm{d_s}\mathbf{u}}{\mathrm{d}t}=q_{\mathrm{a}} \tag{1a}$$

$$\frac{\mathrm{d_s}}{\mathrm{d}t}\left(\rho_{\mathrm{w}}^{\mathrm{l}} S^{\mathrm{l}} \varphi+\rho_{\mathrm{w}}^{\mathrm{g}} S^{\mathrm{g}} \varphi\right)+\nabla\cdot\left(\mathbf{J}_{\mathrm{w}}^{\mathrm{l}}+\mathbf{J}_{\mathrm{w}}^{\mathrm{g}}\right)+\rho_{\mathrm{w}}^{\mathrm{l}} S^{\mathrm{l}} \varphi \nabla\cdot\frac{\mathrm{d_s}\mathbf{u}}{\mathrm{d}t}=q_{\mathrm{w}} \tag{1b}$$

where $\frac{\mathrm{d_s}}{\mathrm{d}t}$ denotes the material time derivative following the solid skeleton, ∇ is the

Nabla operator, $\rho_{\mathrm{a}}^{\mathrm{g}}$, $\rho_{\mathrm{w}}^{\mathrm{l}}$ and $\rho_{\mathrm{w}}^{\mathrm{g}}$ represent the density of dry air, liquid water and vapor respectively. S^{g} and S^{l} denote the saturation of gas and liquid phase. φ refers to the porosity. $\mathbf{J}_{\mathrm{a}}^{\mathrm{g}}$ is the air flux while $\mathbf{J}_{\mathrm{w}}^{\mathrm{l}}$ and $\mathbf{J}_{\mathrm{w}}^{\mathrm{g}}$ are liquid water and vapor flux respectively. $\mathbf{u}$ represents the soil displacements, with and q_{a} and q_{w} are the source terms of air and water, following the definition in Eqs. (6a) and (6b) respectively.

2.1.2 Energy conservation equation

The total energy conservation equation over all phases reads as follows (Wang *et al.*, 2015):

$$\left(C^{\mathrm{s}}\rho^{\mathrm{s}}(1-\varphi)+C^{\mathrm{l}}\rho^{\mathrm{l}}S^{\mathrm{l}}\varphi+C^{\mathrm{g}}\rho^{\mathrm{g}}S^{\mathrm{g}}\varphi+C^{\mathrm{h}}\rho^{\mathrm{h}}S^{\mathrm{h}}\varphi\right)\frac{\mathrm{d_s}T}{\mathrm{d}t}+\nabla\cdot\mathbf{J}_{\mathrm{c}}+\nabla\cdot\left(\mathbf{J}_{\mathrm{E}}^{\mathrm{l}}+\mathbf{J}_{\mathrm{E}}^{\mathrm{g}}\right)=q_{\mathrm{E}} \quad (2)$$

whereC^{s}, C^{l}, C^{g} and C^{h} are the specific heat capacity of soil, liquid, gas and NGHs respectively. $\mathbf{J}_{\mathrm{c}}$ refers to the heat flux of conduction, $\mathbf{J}_{\mathrm{E}}^{\mathrm{l}}$ and $\mathbf{J}_{\mathrm{E}}^{\mathrm{g}}$ denote the heat advection fluxes caused by liquid and gas migrations. The source terms of energy q_{E} is regulated by Eq. (6d).

2.1.3 Momentum balance equation

Neglecting the inertial forces and considering the gravity effect, the linear momentum balance equation for all phases is governed by (Wang *et al.*, 2015):

$$\nabla\cdot\boldsymbol{\sigma}+\left(\rho^{\mathrm{s}}(1-\varphi)+\rho^{\mathrm{l}}S^{\mathrm{l}}\varphi+\rho^{\mathrm{g}}S^{\mathrm{g}}\varphi+\rho^{\mathrm{h}}S^{\mathrm{h}}\varphi\right)\mathbf{g}=\mathbf{0} \quad (3)$$

where $\mathbf{g}$ is the gravity vector, and $\boldsymbol{\sigma}$ is the total stress tensor, which is related to the effective stress tensor $\boldsymbol{\sigma}'$ by (Sun *et al.*, 2019):

$$\boldsymbol{\sigma}=\boldsymbol{\sigma}'-\frac{S^{\mathrm{l}}p^{\mathrm{l}}+S^{\mathrm{g}}p^{\mathrm{g}}}{S^{\mathrm{l}}+S^{\mathrm{g}}}\mathbf{1}=\boldsymbol{\sigma}'-\frac{S^{\mathrm{g}}}{S^{\mathrm{l}}+S^{\mathrm{g}}}p^{\mathrm{g}}\mathbf{1}-\frac{S^{\mathrm{l}}}{S^{\mathrm{l}}+S^{\mathrm{g}}}p^{\mathrm{l}}\mathbf{1} \quad (4)$$

where **1** is the second-order identity tensor.

2.2 Constitutive equations

2.2.1 NGH dissociation

During the NGH dissociation, the solid NGH transforms to liquid water and methane gas, changing properties of the solid skeleton. Meanwhile, it absorbs a large amount of heat. At 275.15 K, this is approximate 409.63 kJ per kilogram of NGHs (Liang *et al*., 2010). Currently, several models haven been proposed for quantitatively describing the NGH dissociation process, mainly including equilibrium model (Kowalsky and Moridis, 2007; Teng and Zhang, 2020), pseudo-kinetic model (Sánchez *et al.*, 2018; Teymouri *et al.*, 2020) and kinetic reaction model (Kim *et al.*, 1987; Yin *et al.*, 2018), whose specific characteristics are shown in Table 1.

Table 1 NGH dissociation models

Dissociation model	Characteristics	Reference
Equilibrium model	NGH dissociates completely once phase equilibrium state no longer holds	Kowalsky and Moridis (2007) Teng and Zhang (2020)
Pseudo-kinetic model	The rate of NGH dissociation is determined by the dimensionless distance away from the *p*-*T* plane	Sánchez *et al*. (2018) Teymouri *et al*. (2020)
Kinetic reaction model	The rate of NGH dissociation originates from chemical kinetic theory and is affected by *p* and *T*	Kim *et al*. (1987) Yin *et al*. (2018)

To our best of knowledge, the Kim-Bishnoi kinetic reaction model is the most widely applied. Based on the kinetic chemical reaction theory, the activation energy and the specific surface area are considered to be the factor determining the actual reaction rate. The dissociation rate then reads:

$$R_r = K_d A_s (p^e - p^g) \tag{5a}$$

$$K_d = K_0 \exp\left(-\frac{\Delta E}{RT}\right) \tag{5b}$$

where R_r refers to the reaction rate, K_d is the kinetic dissociation rate, K_0 is the kinetic dissociation constant, ΔE is the activation energy, R is the gas constant, and A_s is the specific surface area, which can be given by $A_s = \varphi A_{s0} S^h$, where S^h is NGH saturation and $A_{s0} = 7.5 \times 10^5\ \mathrm{m}^{-1}$ (Hardwick and Mathias, 2018; Sun *et al*., 2019). With the dissociation rate calculated in Eqs. (5a) and (5b), the source terms for air, water, NGH and energy equations read:

$$q_a = M_a R_r \tag{6a}$$

$$q_w = N_h M_w R_r \tag{6b}$$

$$q_h = -M_h R_r \tag{6c}$$

$$q_E = -\Delta H M_h R_r \tag{6d}$$

where q_h is the source terms for the NGH equation, M_a, M_w and M_h are the molar mass for air, water and NGH, N_h is the stoichiometric ratio of molar water amount over that of dissociated methane. ΔH is the enthalpy change, which is usually expressed as the linear function of T (Liang *et al*., 2010; Sun *et al*., 2019):

$$\Delta H = C_0 + C_1 T \tag{7}$$

where C_0 and C_1 are parameters of enthalpy change.

Concerning that the Kim-Bishnoi model is well studied and also verified against experimental data, it is adopted in this work to calculate kinetic reaction rates.

2.2.2 Fluid migration

Pore fluids here refer to pore gases (dry air and water vapor) and pore water, and the migrating process of pore gases includes both advection and diffusion (Wang *et al*., 2015). The corresponding processes are regulated:

$$\mathbf{J}_\alpha^{\mathrm{g}}=\mathbf{J}_{\alpha\mathrm{C}}^{\mathrm{g}}+\mathbf{J}_{\alpha\mathrm{D}}^{\mathrm{g}} \quad \alpha=\mathrm{a,\,w} \tag{8}$$

where α represent component of pore gases, and $\mathbf{J}_{\alpha\mathrm{C}}^{\mathrm{g}}$ and $\mathbf{J}_{\alpha\mathrm{D}}^{\mathrm{g}}$ are respectively the advection and diffusing parts for the α phase respectively. They can be determined by Darcy's law and Fick's law (Wang *et al*., 2015):

$$\mathbf{J}_{\alpha\mathrm{C}}^{\mathrm{g}}=-\frac{\rho_\alpha^{\mathrm{g}}\mathbf{K}k_{\mathrm{rel}}^{\mathrm{g}}}{\mu^{\mathrm{g}}}\left(\nabla p^{\mathrm{g}}-\rho^{\mathrm{g}}\mathbf{g}\right) \quad \alpha=\mathrm{a,\,w} \tag{9a}$$

$$\mathbf{J}_{\alpha\mathrm{D}}^{\mathrm{g}}=-\rho^{\mathrm{g}}\frac{M_{\mathrm{a}}M_{\mathrm{w}}}{\left(M_{\mathrm{g}}\right)^2}\mathbf{D}_\alpha^{\mathrm{g}}\nabla\left(\frac{p_\alpha^{\mathrm{g}}}{p^{\mathrm{g}}}\right) \quad \alpha=\mathrm{a,\,w} \tag{9b}$$

For pore water, Darcy's law is considered:

$$\mathbf{J}_{\mathrm{w}}^{\mathrm{l}}=-\frac{\rho_{\mathrm{w}}^{\mathrm{l}}\mathbf{K}k_{\mathrm{rel}}^{\mathrm{l}}}{\mu^{\mathrm{l}}}\left(\nabla p^{\mathrm{l}}-\rho_{\mathrm{w}}^{\mathrm{l}}\mathbf{g}\right) \tag{10}$$

where ρ^{g} and M_{g} can be expressed as:

$$\rho^{\mathrm{g}}=\rho_{\mathrm{a}}^{\mathrm{g}}+\rho_{\mathrm{w}}^{\mathrm{g}} \tag{11a}$$

$$\frac{1}{M_{\mathrm{g}}}=\frac{\rho_{\mathrm{w}}^{\mathrm{g}}}{\rho^{\mathrm{g}}}\frac{1}{M_{\mathrm{w}}}+\frac{\rho_{\mathrm{a}}^{\mathrm{g}}}{\rho^{\mathrm{g}}}\frac{1}{M_{\mathrm{a}}} \tag{11b}$$

According to Clapeyron's equation for an ideal gas and Dalton's law for pressure of pore gases, we have:

$$\rho_\alpha^{\mathrm{g}}=\frac{p_\alpha^{\mathrm{g}}M_\alpha}{RT} \quad \alpha=\mathrm{a,\,w} \tag{12a}$$

$$p^{\mathrm{g}}=p_{\mathrm{a}}^{\mathrm{g}}+p_{\mathrm{w}}^{\mathrm{g}} \tag{12b}$$

For vapor pressure $p_{\mathrm{w}}^{\mathrm{g}}$ and saturated vapor pressure $p_{\mathrm{ws}}^{\mathrm{g}}$, the Kalvin-Laplace equation and the model proposed by Philip and De Vries (1957) are applied:

$$p_{\mathrm{w}}^{\mathrm{g}}=p_{\mathrm{ws}}^{\mathrm{g}}\exp\left(-\frac{p^{\mathrm{c}}M_{\mathrm{w}}}{\rho^{\mathrm{l}}RT}\right) \tag{13a}$$

$$p_{\mathrm{ws}}^{\mathrm{g}}=10^{-3}\frac{RT}{M_{\mathrm{w}}}\exp\left(19.84-\frac{4975.9}{T}\right) \tag{13b}$$

where p^{c} is the capillary pressure. According to the Brooks-Corey function for soil water retention curve (SWRC), p^{c} is regulated by the difference between gas and liquid pressure (Liang *et al*., 2010; Sun *et al*., 2019):

$$p^{\mathrm{c}}=p^{\mathrm{g}}-p^{\mathrm{l}} \tag{14a}$$

$$p^{\mathrm{c}}=p^{0}{S_{\mathrm{eff}}}^{-n_{\mathrm{pc}}} \tag{14b}$$

where S_{eff} is the effective saturation, expressed by $S_{\mathrm{eff}}=\frac{\frac{S^{\mathrm{l}}}{S^{\mathrm{l}}+S^{\mathrm{g}}}-S_{\mathrm{rl}}-S_{\mathrm{rg}}}{1-S_{\mathrm{rl}}-S_{\mathrm{rg}}}$, p^{0} is the constant entry air pressure, and n_{pc} is the pore size distribution index.

Relative permeabilities of liquid and gas are given by Corey's model (Corey, 1984; Hardwick and Mathias, 2018; Sun *et al*., 2019):

$$k_{\mathrm{rel}}^{\mathrm{g}}=\left(\frac{S^{\mathrm{g}}-S_{\mathrm{rg}}}{1-S_{\mathrm{rg}}}\right)^{n_{\mathrm{g}}} \tag{15a}$$

$$k_{\mathrm{rel}}^{\mathrm{l}}=\left(\frac{S^{\mathrm{l}}-S_{\mathrm{rl}}}{1-S_{\mathrm{rl}}}\right)^{n_{\mathrm{l}}} \tag{15b}$$

where S_{rg} and S_{rl} are the residual saturation of gas and liquid phase, and n_{g} and n_{l} are the pore size distribution index.

The permeability of hydrate-bearing sediments is highly associated with porosity and NGH saturation, and a critical threshold permeability model has been proposed by Sun *et al.* (2019) and Hardwick and Mathias (2018) to more accurately reflect the relatively slow far-field boundary pressure response:

$$K=\begin{cases} K_0\left(\frac{\varphi}{\varphi_0}\right)^{\frac{3}{2}}\left(\frac{1-\varphi}{1-\varphi_0}\right)^3\left(1-S_0^{\mathrm{h}}\right)^{N_{\mathrm{p}}} & S^{\mathrm{h}}>S_{\mathrm{c}}^{\mathrm{h}} \\ K_0\left(\frac{\varphi}{\varphi_0}\right)^{\frac{3}{2}}\left(\frac{1-\varphi}{1-\varphi_0}\right)^3\left(1-\frac{S^{\mathrm{h}}}{S_{\mathrm{c}}^{\mathrm{h}}}\left(1-\left(1-S_0^{\mathrm{h}}\right)^{N_{\mathrm{p}}}\right)\right) & S^{\mathrm{h}}<S_{\mathrm{c}}^{\mathrm{h}} \end{cases} \quad (16)$$

where K is the scalar value of permeability tensor $\mathbf{K}$ in isotropic soil, K_0, φ_0 and S_0^{h} are the initial intrinsic permeability, porosity and NGH saturation of the host sediments, and N_{p} and $S_{\mathrm{c}}^{\mathrm{h}}$ are parameters related to the impact of NGH for the permeability model.

2.2.3 Heat transfer

The heat transfer process consists of heat conduction and advection, with the former often described by Fourier's law with the volume average model for heat conduction coefficient tensor (Sun *et al*., 2019):

$$\mathbf{J}_{\mathrm{c}} = -\left(\mathbf{k}^{\mathrm{s}}(1-\varphi) + \mathbf{k}^{\mathrm{l}}S^{\mathrm{l}}\varphi + \mathbf{k}^{\mathrm{g}}S^{\mathrm{g}}\varphi + \mathbf{k}^{\mathrm{h}}S^{\mathrm{h}}\varphi\right)\nabla T \quad (17)$$

where $\mathbf{k}^{\mathrm{s}}$, $\mathbf{k}^{\mathrm{l}}$, $\mathbf{k}^{\mathrm{g}}$ and $\mathbf{k}^{\mathrm{h}}$ are the heat conductive coefficient tensor of soil, liquid, gas and NGHs respectively.

Furthermore, the heat advection flux for liquid and gas phase is formulated as:

$$\mathbf{J}_{\mathrm{E}}^{\mathrm{l}} = C^{\mathrm{l}}\rho^{\mathrm{l}}\mathbf{v}^{\mathrm{l}}T \quad (18a)$$

$$\mathbf{J}_{\mathrm{E}}^{\mathrm{g}} = C^{\mathrm{g}}\rho^{\mathrm{g}}\mathbf{v}^{\mathrm{g}}T \quad (18b)$$

where the Darcy velocity $\mathbf{v}^{\mathrm{l}}$ and $\mathbf{v}^{\mathrm{g}}$ can be obtained from Darcy's law by Eq. (9a) and Eq. (10).

2.2.4 skeleton deformation

The skeleton deformation is determined by the soil constitutive relationship, which is highly affected by the NGH dissociation. Generally, the strengthening effect of NGH existence and weakening effect of NGH dissociation on soil skeleton are both linked to NGH saturation S^h. In the literature, the deformation of hydrate-bearing sediments can be described by linear elasticity, nonlinear elasticity, elastic-plasticity, elasto-viscoplasticity, critical state mechanics, and etc. Following the categorization of the mechanical constitutive model, the representative codes and references are summarized in Table 2.

Table 2 Soil constitutive models and representative codes

Constitutive model	Representative code	Reference
Linear elasticity	Comsol	Sun *et al.*, 2019
	DUNE-PDELab	Gupta *et al.*, 2015
	K+hydrate+Flac	Kim *et al.*, 2018
	GrapeFloater	Liu *et al.*, 2017
Linear elasticity with Drucker-Prager	Tough+Hydrate+Millstone	Moridis *et al.*, 2019
	DUNE-PDELab	Parente *et al.*, 2019
Linear elasticity with Mohr-Coulomb	Tough+Hydrate+Flac	Rutqvist *et al.*, 2009
	Tough+Hydrate+Biot	Jin *et al.*, 2018a
	K+hydrate+Flac	Klar *et al.*, 2013
	STARS	Wu and Hsieh, 2020
	Abaqus	Song *et al.*, 2019
Nonlinear elasticity (Duncan-Chang model)	Abaqus	Zhao and Shang, 2010
Elasto-viscoplasticity	COMVI-MH	Kimoto *et al.*, 2007, 2010

Critical soil mechanics	Code-bright	De La Fuente *et al.*, 2020
	Comsol	Sun *et al.*, 2018, 2019
	Geo-COUS	Shin and Santamarina, 2017, 2019
	CMHGS	Zhou *et al.*, 2020

For modified linear elasticity (Santamarina and Ruppel, 2010; Gupta *et al.*, 2015; Sun *et al.*, 2019), triaxial tests reveal that S^{h} have a great impact on elastic modulus but little impact on Poisson's ratio. Due to fewer parameters and easier calibration, this model can be implemented into numerical simulator and possesses good convergence. The modified model proposed by Santamarina and Ruppel (2010) can be expressed as:

$$E=E_0\left(\frac{\sigma_{\mathrm{c}}}{\sigma_{\mathrm{c0}}}\right)^{\mathrm{a_h}}+c_{\mathrm{h}}E_{\mathrm{h}}\left(S^{\mathrm{h}}\right)^{\mathrm{b_h}} \tag{19}$$

where E is the modified elastic modulus, σ_{c} and σ_{c0} are the confining pressure and its initial value respectively. E_0 and E_{h} refer to the soil modulus without NGHs and enhanced modulus by pure NGHs. $\mathrm{a_h}$ is the sensitivity of the modulus of hydrate-free sand to confining stress σ_{c}, $\mathrm{b_h}$ is the nonlinear effect of NGH saturation, and c_{h} is the contribution of the isothermal modulus of hydrate for a given pore habit.

Since the focuses of this study are on the gas-liquid migration and gas production efficiency during the NGH dissociation, modified elastic model is implemented into the OGS for convenience and better convergence. The modified linear elasticity relationship thus reads:

$$\boldsymbol{\sigma}' = \mathbf{D}^{\mathbf{e}}{:}(\boldsymbol{\varepsilon}-\boldsymbol{\varepsilon}_T) = \mathbf{D}^{\mathbf{e}}{:}\frac{\nabla\mathbf{u}+\nabla^{\mathrm{T}}\mathbf{u}}{2} - \mathbf{D}^{\mathbf{e}}{:}\mathbf{1}\alpha^{\mathrm{s}}(T-\mathrm{T}_0) \tag{20}$$

where $\mathbf{D}^{\mathbf{e}}$ is the linear elastic tensor, which can be determined by Modified elastic modulus E following Eq. (19), together with Poisson's ratio ν. Here $\boldsymbol{\varepsilon}$ and $\boldsymbol{\varepsilon}_T$ refer to the total and thermal strain tensors. α^{s} is the linear thermal expansion coefficient of the solid skeleton, and T_0 denotes the initial temperature in Kelvin.

Considering the above-mentioned coupled processes, this model is suited for cases within small strains (Gupta *et al*., 2015), where the range of application is limited to small-strain cases far away from the critical state (Masui *et al*., 2006; Miyazaki *et al*., 2011). For those situations where large strains or plastic failures occur, soil constitutive relationships accounting for behavior of nonlinear elasticity (Zhao and Shang, 2010; Miyazaki *et al*., 2011), elastic-plasticity (Rutqvist et al., 2009; Moridis *et al*., 2019), critical state mechanics (Sun *et al.*, 2018; De La Fuente *et al*., 2020) or others (Kimoto *et al.*, 2007) should be considered. These sophisticated models will be further investigated in our future work to have a deep discussion about hydrate related geotechnical hazards (Maslin *et al*., 2010; McConnell *et al*., 2012).

3 Numerical model developments

3.1 Establishment of NGH dissociation process considering gravity effect

3.1.1 Numerical description for NGH dissociation process

In this study, the open-source FEM platform OGS (Kolditz *et al*., 2012; Lehmann *et al*., 2018; Bilke *et al*., 2019) has been adopted, which is developed in C++ to solve multiphase coupled problems and currently in its 6th version (hereafter as OGS-6, Lehmann *et al*., 2018; Bilke *et al*., 2019). Compared with the former 5-th version (Kolditz *et al*., 2012, 2016), both the input files and source codes are clearer and more concise in OGS-6. This makes the source code of OGS-6 easier and more convenient to be modified for users or developers who have a specific requirement, and even establish their own models. Additionally, more third-party libraries have been included in OGS-6 for more flexible extension of additional features, such as Paraview for post-processing and ogs6py for python-API of OGS. The MFront library for soil constitutive relationship and the python script for complex boundary conditions are also embedded. Considering these advantages, OGS-6 is used in this study.

In OGS-6, four partial differential equations, including Eqs. (1a), (1b), (2) and (3), are solved for four primary variables, i.e. $\mathbf{X}=[p^{\mathrm{g}} \quad p^{\mathrm{l}} \quad T \quad \mathbf{u}]^{\mathrm{T}}$. The model domain is spatially discretized with finite element method, while backward Euler finite difference approach is applied to discretize the time. The NGH dissociation process is in-cooperated into the governing equations via source terms, based on the calculated NGH reaction rate (Eqs. (6a), (6b), (6c) and (6d)). As the reaction rate is highly sensitive to the primary variables, minor changes in the $\mathbf{X}$ vector can lead to considerable amount of source and sink terms, causing instability and non-convergence issue in certain time steps. To mitigate this problem, the NGH reaction rate is expanded in Taylor series, and a first-order approximation is calculated based on the primary variable vector $\mathbf{X}$ from the previous iteration. The updated reaction rate thus reads:

$$R_{\mathrm{r}}(\mathbf{X})=R_{\mathrm{r}}(\mathbf{X}_0)+\frac{\partial R_{\mathrm{r}}(\mathbf{X}_0)}{\partial \mathbf{X}}\cdot(\mathbf{X}-\mathbf{X}_0) \tag{21a}$$

$$\frac{\partial R_{\mathrm{r}}}{\partial p^{\mathrm{g}}}=-K_{\mathrm{d}}A_{\mathrm{s}} \tag{21b}$$

$$\frac{\partial R_{\mathrm{r}}}{\partial T}=K_{\mathrm{d}}A_{\mathrm{s}}\left(\frac{\Delta E}{RT^2}(p^{\mathrm{e}}-p^{\mathrm{g}})+\frac{9459}{T^2}p^{\mathrm{e}}\right) \tag{21c}$$

$$\frac{\partial R_{\mathrm{r}}(\mathbf{X}_0)}{\partial \mathbf{X}}=\left[\frac{\partial R_{\mathrm{r}}}{\partial p^{\mathrm{g}}} \quad 0 \quad \frac{\partial R_{\mathrm{r}}}{\partial T} \quad \mathbf{0}\right]\Bigg|_{\mathbf{X}=\mathbf{X}_0} \tag{21d}$$

Subsequently, the source terms in the governing equations are substituted by the expanded $R_{\mathrm{r}}(\mathbf{X})$ following Eq. (21a). Similar to the solid phase mass equations in **Appendix I**, the mass equation for NGH components can be expanded as:

$$\rho^{\mathrm{h}} S^{\mathrm{h}} \frac{\partial \varphi}{\partial t} + \varphi \rho^{\mathrm{h}} \frac{\partial S^{\mathrm{h}}}{\partial t} + \varphi \rho^{\mathrm{h}} S^{\mathrm{h}} \left(\frac{1}{\rho^{\mathrm{h}}} \frac{\partial \rho^{\mathrm{h}}}{\partial t} \right) + \rho^{\mathrm{h}} S^{\mathrm{h}} \varphi \frac{\mathrm{d}_{\mathrm{s}}(\nabla \cdot \mathbf{u})}{\mathrm{d}t} = q_{\mathrm{h}} \tag{22}$$

For the local problem, the value of S^{h} needs to be found based on the given primary variables. With a given time step size, the $\frac{\partial \varphi}{\partial t}$, $\frac{\partial \rho^{\mathrm{h}}}{\partial t}$ and $\frac{\mathrm{d}_{\mathrm{s}}(\nabla \cdot \mathbf{u})}{\mathrm{d}t}$ terms can be substituted by the finite difference of primary variables over time. This transforms Eq. (22) to an ordinary differential equation of S^{h} over time. By fixing primary variable values from the last iteration, the reaction rate R_{r} is then implicitly dependent on the NGH saturation S^{h}:

$$R_{\mathrm{r}}(\mathbf{X}_0) = R_{\mathrm{r}}\left(\mathbf{X}_0, S^{\mathrm{h}}_{t-\Delta t}\right) + \frac{\partial R_{\mathrm{r}}\left(\mathbf{X}_0, S^{\mathrm{h}}_{t-\Delta t}\right)}{\partial S^{\mathrm{h}}} \cdot \left(S^{\mathrm{h}}_t - S^{\mathrm{h}}_{t-\Delta t}\right) \tag{23}$$

where the subscript t and Δt refers to the current time and time step size. Therefore, the explicit expression of S^{h} over time can be written as:

$$S^{\mathrm{h}}_t = \frac{\varphi S^{\mathrm{h}}_{t-\Delta t} + \frac{M_{\mathrm{h}}}{\rho^{\mathrm{h}}} \frac{\partial R_{\mathrm{r}}\left(\mathbf{x}_0, S^{\mathrm{h}}_{t-\Delta t}\right)}{\partial S^{\mathrm{h}}} \Delta t S^{\mathrm{h}}_{t-\Delta t} - \frac{M_{\mathrm{h}}}{\rho^{\mathrm{h}}} R_{\mathrm{r}}\left(\mathbf{x}_0, S^{\mathrm{h}}_{t-\Delta t}\right) \Delta t}{\left(\varphi + \frac{M_{\mathrm{h}}}{\rho^{\mathrm{h}}} \frac{\partial R_{\mathrm{r}}\left(\mathbf{x}_0, S^{\mathrm{h}}_{t-\Delta t}\right)}{\partial S^{\mathrm{h}}} \Delta t + \left(-(1-\varphi)\beta_{\mathrm{s}} - \varphi \beta_{\mathrm{h}}\right)(T_t - T_{t-\Delta t}) + ((\varepsilon_{\mathrm{V}})_t - (\varepsilon_{\mathrm{V}})_{t-\Delta t}) \right)} \tag{24}$$

When NGHs completely dissociate in a time step Δt, the actual reaction time $\Delta t_{\mathrm{react}}$ can be calculated by:

$$\Delta t_{\mathrm{react}} = \frac{\varphi \rho^{\mathrm{h}} S^{\mathrm{h}}_{t-\Delta t}}{M_{\mathrm{h}} \left(R_{\mathrm{r}}\left(\mathbf{x}_0, S^{\mathrm{h}}_{t-\Delta t}\right) - \frac{\partial R_{\mathrm{r}}\left(\mathbf{x}_0, S^{\mathrm{h}}_{t-\Delta t}\right)}{\partial S^{\mathrm{h}}} S^{\mathrm{h}}_{t-\Delta t} \right)} \tag{25}$$

Similar to S^{h}, the explicit expression of φ is derived from the solid mass equation according to **Appendix I**. Its explicit form in a certain iteration reads:

$$\varphi_t = \frac{\varphi_{t-\Delta t} - \beta_{\mathrm{s}}(T_t - T_{t-\Delta t}) + ((\varepsilon_{\mathrm{V}})_t - (\varepsilon_{\mathrm{V}})_{t-\Delta t})}{1 - \beta_{\mathrm{s}}(T_t - T_{t-\Delta t}) + ((\varepsilon_{\mathrm{V}})_t - (\varepsilon_{\mathrm{V}})_{t-\Delta t})} \tag{26}$$

The first-order term of the Taylor series uses the primary variable values from the previous iteration. This allows a higher numerical stability and efficiency, especially when the fast-changing reaction rates have to be included.

3.1.2 Numerical implementation of NGH dissociation into OGS

Based on the OGS-6 (Kolditz *et al*., 2012; Lehmann *et al*., 2018; Bilke *et al*., 2019), the existing THM model is extended in this work by implementing an additional air mass balance equation to reflect the partially saturated condition (Zhu *et al*., 2021). In detail, Dalton’s law of partial pressure, Clapeyron’s equation of ideal gas, Kelvin-Laplace equation, and saturated vapor pressure equation are adopted to illustrated gas-liquid migration. In the extended model, a critical threshold permeability model (Hardwick and Mathias, 2018; Sun *et al*., 2019) is applied to the gas / liquid phase, which is dependent on the porosity and NGH saturation. The NGH dissociation process is modeled by introducing phase equilibrium equation, chemical kinetic reaction rate, mass / energy rate and enthalpy change, which are incorporated into the governing equations via source terms, following Eqs. (6a) to (6d). Before the start of the simulation, a pre-calculation is performed to find the initial steady-state pressure, temperature and stress field, with the gravity effect taken into consideration. The distributions of these three variables are set as initial conditions. Within each iteration, the secondary state variables, such as hydrate saturation and porosity, are updated according to the current time step primary variable values.

The flux boundary conditions for air, water and energy equations, and traction boundary condition for the stresses are:

$$(\mathbf{J}_{\mathrm{a}}^{\mathrm{g}})\cdot\mathbf{n} = q^{\mathrm{a}} \ \text{ on } \ \Gamma_{\mathrm{a}}^{q} \tag{27a}$$

$$\left(\mathbf{J}_{\mathrm{w}}^{\mathrm{l}} + \mathbf{J}_{\mathrm{w}}^{\mathrm{g}}\right)\cdot\mathbf{n} = q^{\mathrm{w}} \ \text{ on } \ \Gamma_{\mathrm{w}}^{q} \tag{27b}$$

$$(\mathbf{J}_{\mathrm{c}})\cdot\mathbf{n} = q^{\mathrm{E}} + \alpha_{\mathrm{c}}(T_{\mathrm{c}} - T) \ \text{ on } \ \Gamma_{\mathrm{E}}^{q} \tag{27c}$$

$$\boldsymbol{\sigma}\cdot\mathbf{n} = \bar{\mathbf{t}} \ \text{ on } \ \Gamma_{\mathbf{u}}^{q} \tag{27d}$$

where q^{a}, q^{w} and q^{E} are the air, water and energy flux across the boundaries, Γ_{a}^{q}, Γ_{w}^{q}, Γ_{E}^{q} and $\Gamma_{\mathbf{u}}^{q}$ are the respective Neumann boundaries, $\bar{\mathbf{t}}$ is the traction vector on $\Gamma_{\mathbf{u}}^{q}$, $\mathbf{n}$ is the unit normal vector, α_{c} is the heat exchange coefficient, and T_{c} is the circumstantial temperature, which can be used to represent the air and water bath technology used in NGH extraction (Hardwick and Mathias, 2018; Sun *et al*., 2019).

In the finite element setting, the p^{g}, p^{l}, T and $\mathbf{u}$ values on the integration points are obtained by multiplying nodal primary variable vectors ($\overline{\mathbf{p}^{\mathrm{g}}}$, $\overline{\mathbf{p}^{\mathrm{l}}}$, $\overline{\mathbf{T}}$, $\overline{\mathbf{u}}$) and the shape function matrices $\mathbf{N}$. The Bubnov-Galerkin procedure for the construction of the weak form of Eqs. (1a), (1b), (2) and (3) is applied to formulate the global linear equation system. Eventually, the following asymmetric, non-linear and coupled system of equations are obtained:

$$\begin{bmatrix} \mathbf{M}_{\mathrm{gg}} & \mathbf{M}_{\mathrm{gl}} & \mathbf{M}_{\mathrm{gT}} & \mathbf{M}_{\mathrm{gu}} \\ \mathbf{M}_{\mathrm{lg}} & \mathbf{M}_{\mathrm{ll}} & \mathbf{M}_{\mathrm{lT}} & \mathbf{M}_{\mathrm{lu}} \\ \mathbf{0} & \mathbf{0} & \mathbf{M}_{\mathrm{TT}} & \mathbf{0} \\ \mathbf{0} & \mathbf{0} & \mathbf{0} & \mathbf{0} \end{bmatrix} \frac{\partial}{\partial \mathrm{t}} \begin{bmatrix} \overline{\mathbf{p}^{\mathrm{g}}} \\ \overline{\mathbf{p}^{\mathrm{l}}} \\ \overline{\mathbf{T}} \\ \overline{\mathbf{u}} \end{bmatrix} + \begin{bmatrix} \mathbf{K}_{\mathrm{gg}} & \mathbf{K}_{\mathrm{gc}} & \mathbf{K}_{\mathrm{gT}} & \mathbf{0} \\ \mathbf{K}_{\mathrm{lg}} & \mathbf{K}_{\mathrm{ll}} & \mathbf{K}_{\mathrm{lT}} & \mathbf{0} \\ \mathbf{K}_{\mathrm{Tg}} & \mathbf{K}_{\mathrm{Tl}} & \mathbf{K}_{\mathrm{TT}} & \mathbf{0} \\ \mathbf{K}_{\mathrm{ug}} & \mathbf{K}_{\mathrm{ul}} & \mathbf{K}_{\mathrm{uT}} & \mathbf{K}_{\mathrm{uu}} \end{bmatrix} \begin{bmatrix} \overline{\mathbf{p}^{\mathrm{g}}} \\ \overline{\mathbf{p}^{\mathrm{l}}} \\ \overline{\mathbf{T}} \\ \overline{\mathbf{u}} \end{bmatrix} = \begin{bmatrix} \mathbf{f}_{\mathrm{g}} \\ \mathbf{f}_{\mathrm{l}} \\ \mathbf{f}_{\mathrm{T}} \\ \mathbf{f}_{\mathrm{u}} \end{bmatrix} \tag{28}$$

where explicit expressions of matrices, $\mathbf{M}_{\mathrm{ij}}$, $\mathbf{K}_{\mathrm{ij}}$ and $\mathbf{f}_{\mathrm{i}}$ are provided in **Appendix II**; here i, j $\in$ {p, T, u}.

The solution strategy of solving the coupled THCM model considering NGH dissociation is illustrated in Fig. 3. The coupled model is solved in a monolithic scheme. Non-linear iteration is regulated by the Newton-Raphson method. Within each non-linear iteration, the linear equation system is solved with the Biconjugate gradient stabilized (BICGSTAB) approach (Van der Vorst, 1992). The overall strategy is as follows: (1) following the NGH kinetic reaction equation and phase equilibrium equation, the reaction rates of NGHs, liquid, gas and energy are calculated and applied in source terms of mass and energy equations; (2) based on soil and NGH mass equations, φ and S^{h} are solved in each iteration respectively, their impacts on the soil stuffiness are then considered; (3) the Kalvin-Laplace equation, Dalton's partial pressure law, Clapeyron's equation, saturated vapor pressure equation and critical threshold permeability model for intrinsic permeability and Corey's model for relative permeability are adopted to capture the saturation, density and partial pressure for liquid and gas phases; (4) when considering gravity, the initial gas / liquid pressure and stress distribution are obtained by pre-calculation. Then they are set as the initial states for the model simulation.

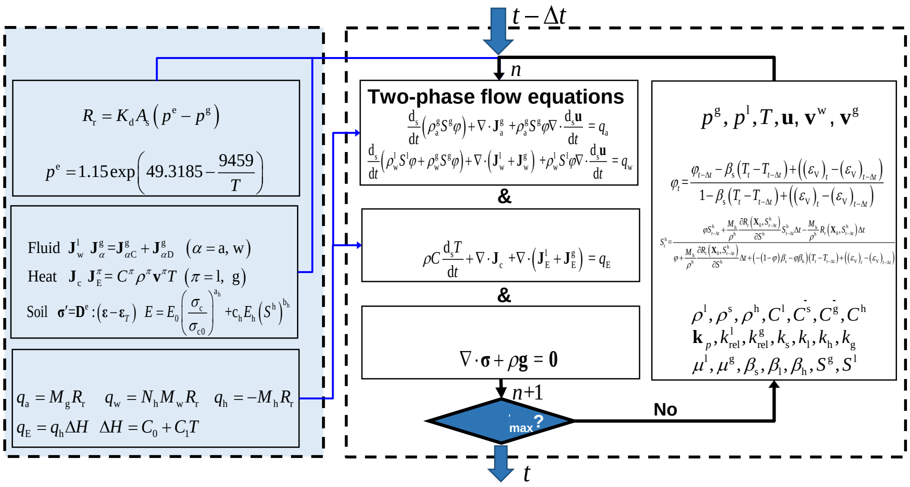

Fig. 3 The strategy of solving THCM coupled model induced by NGH dissociation in OGS-6

3.2 Model verification

In this section, two benchmarks are introduced to verify the aforementioned THCM coupled model. The first one was presented by Schrefler *et al*. (1995) to capture the THM coupled behavior for partial saturated sediments. The secondary one carried out by Masuda *et al*. (1999) in order to explore the THC coupled response during the NGH dissociation by depressurization method.

3.2.1 Benchmark of THM process

Schrefler *et al*. (1995) has proposed a numerical benchmark for the one-dimensional THM coupled response of unsaturated soil, and simulated it with their Comes-Geo code. The model domain has a height of 0.1 m and a width of 0.01 m. The lateral and bottom boundaries are thermally insulated, hydraulically impermeable and simply supported. The initial values for temperature T_0, pore gas pressure p_0^{g}, and pore water pressure p_0^{l} are 283.15 K, 102 kPa and -420 kPa respectively. A temperature increment of 15 K and water pressure decrement of 140 kPa are applied on the top boundary to represent unsaturated subgrade soil below a highway or airfield pavement due to the effect of environmental change. Based on the extended THCM model with NGH dissociation implemented in OGS-6, the S^{h} value is set to zero throughout the simulation. Brooks-Corey model for SWRC and ven Genuchten model for gas / liquid relative permeability are adopted, where $p^{\mathrm{c}} = p^0 S_{\mathrm{eff}}^{1/n_{\mathrm{pc}}}$, p^0=200 kPa , $n_{\mathrm{pc}} = 0.38$, S_{rl}=0.32 S_{rg}=0.0 , $k_{\mathrm{rel}}^{\mathrm{g}}$=$S_{\mathrm{eff}}^{1/2}\left(1-\left(1-S_{\mathrm{eff}}^{1/n_{\mathrm{l}}}\right)^{n_{\mathrm{l}}}\right)^2$, $k_{\mathrm{rel}}^{\mathrm{l}}$=$(1-S_{\mathrm{eff}})^{1/3}\left(1-S_{\mathrm{eff}}^{n_{\mathrm{g}}}\right)^{2n_{\mathrm{g}}}$ and $n_{\mathrm{l}} = n_{\mathrm{g}} = 3.0$. Young's modulus E and Poisson's ratio v of the soil were 6000 kPa and 0.4 respectively, and other details are referred to existing studies (Schrefler *et al*., 1995; Zhu *et al*., 2020).

As is shown in Fig. 4(a), the distribution curves of temperature between Schrefler *et al*. (1995), Zhu *et al*. (2020) with OGS-5 and the current model with OGS-6 are in good agreement. Generally, good consistency of gas pressure can be seen in Fig. 4(b), where only negligible difference can be found between this study and Zhu *et al.* (2020). The minor deviation is caused by the solid and water compressibility considered in OGS-5, which has not been yet included in OGS-6. Besides, differences in gas pressure can be observed at the height about 0.09 m, where the results from Schrefler's (1995) simulation are considerably higher. This is induced by the temperature dependent model for SWRC applied in Schrefler's simulation, and additionally different spatial and temporal discretization. Overall, the newly developed THCM model in OGS-6 is successfully verified to simulate the THM coupled problems in unsaturated sediments.

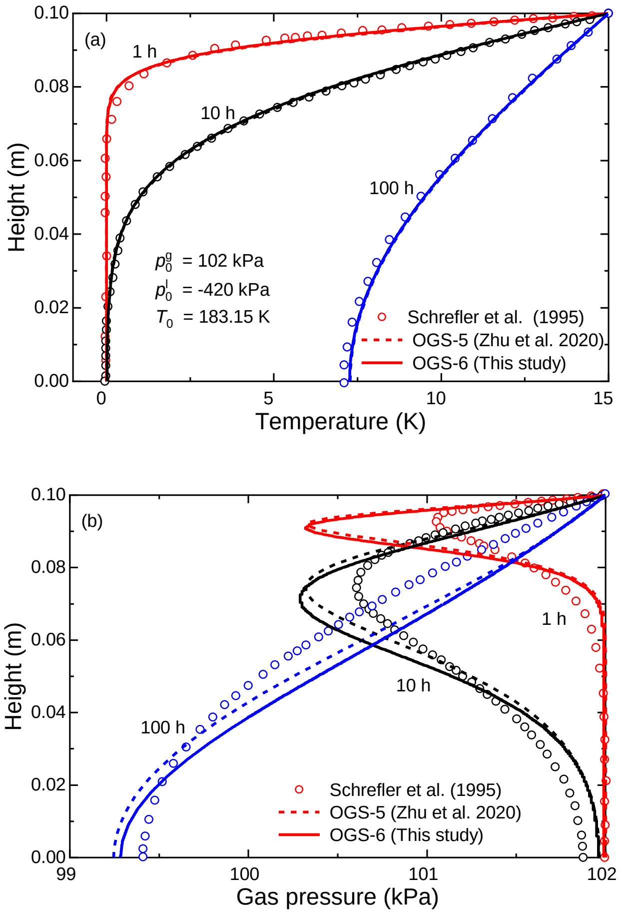

Fig. 4 Comparison of profiles of (a) temperature; (b) gas pressure simulated by the OGS-6 model, by Zhu *et al*. (2020) and by Schrefler *et al*. (1995)

3.2.2 Benchmark of axisymmetric THC process

Masuda *et al.* (1999) has conducted a laboratory-scale test to investigate the behavior of hydrate-bearing sediments during the NGH dissociation under depressurization conditions. His results have been widely applied to verify numerical models (Hardwick and Mathias, 2018; Sun *et al*., 2019; Deng *et al*., 2020). The parameters used here, including capillary pressure, intrinsic permeability, elastic modulus, enthalpy change and common parameters of all phases, can be found in Table 3. The initial conditions are shown in Table 4.

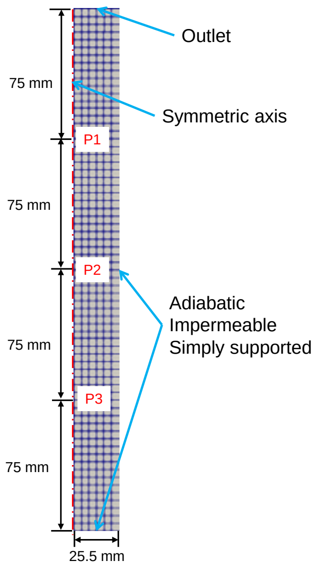

Fig. 5 Domain and mesh of the Masuda's benchmark

Table 3 Parameter values applied in the Masuda's benchmark (following Nazridoust and Ahmadi, 2007; Hardwick and Mathias, 2018; Sun *et al.*, 2019)

Parameters	Symbol	Unit	Expression		Value	
Capillary pressure	p^{c}	MPa	$p^{c}=p^{0}{S_{eff}}^{-n_{pc}}$ $S_{eff}=\frac{\frac{S^{l}}{S^{l}+S^{g}}-S_{rl}-S_{rg}}{1-S_{rl}-S_{rg}}$		p^{0}=1 MPa, n_{pc}=0.65 S_{rl}=0.1, S_{rg}=0.0	
Intrinsic permeability	K	m^2	$K=\begin{cases} K_0\left(\frac{\varphi}{\varphi_0}\right)^{\frac{3}{2}}\left(\frac{1-\varphi}{1-\varphi_0}\right)^{3}\left(1-S_0^{h}\right)^{N_p} & S^{h}>S_c^{h} \\ K_0\left(\frac{\varphi}{\varphi_0}\right)^{\frac{3}{2}}\left(\frac{1-\varphi}{1-\varphi_0}\right)^{3}\left(1-\frac{S^{h}}{S_c^{h}}\left(1-\left(1-S_0^{h}\right)^{N_p}\right)\right) & S^{h}<S_c^{h} \end{cases}$		K_0 = 9.67 × 10^{-4}, φ_0= 0.182 N_p=5.2, S_0^{h}=0.0001	
Elastic modulus	E	MPa	$E=E_0\left(\frac{\sigma_c}{\sigma_{c0}}\right)^{a_h}+c_h E_h\left(S^{h}\right)^{b_h}$		E_0=300, E_h =1350 a_h = 0, b_h = c_h = 1	
Enthalpy change	ΔH	J/kg	$\Delta H = C_0+C_1 T$		C_0=446120 C_1 = −132.638	
			Soil	NGH	Liquid	Gas
Density	ρ^{π}	kg/m^3	2600	910	1000	-
Thermal	k^{π}	W/(m·K)	8.8	0.393	0.556	0.0335

conductivity						
Specific heat capacity	C^{π}	J/(kg·K)	800	2000	4200	2100
Viscosity	μ^{π}	Pa·s	-	-	1×10^{-3}	7×10^{-6}
Thermal expansion	α^{π}	m/K	1.5×10^{-5}	1.5×10^{-5}	4.0×10^{-4}	-
Molar mass	M^{π}	kg/mol	-	0.124	0.018	0.016
Gas constant	R	J/(mol·K)	-	-	-	8.314

Note: π represents s, h, l or g.

Table 4 Initial Conditions in the Masuda's benchmark (following Nazridoust and Ahmadi, 2007; Hardwick and Mathias, 2018; Sun *et al*., 2019)

Variables	Symbol	Unit	Initial value
Temperature	T	K	275.4
Air-bath temperature	T_c	K	275.15
Gas pressure	p^g	MPa	3.75
Outlet pressure	-	MPa	2.84
NGH saturation	S^h	-	0.443
Gas saturation	S^g	-	0.206
Liquid saturation	S^l	-	0.351

As depicted in Figs. 6(a), 6(b) and 6(c), the numerical results for the developed model, such as temperature, gas pressure and volume of gas production, are in close agreement with those observed in the experiment (Masuda *et al.*, 1999) and existing numerical results (Sun *et al.*, 2019). It can be noticed that there exists a slight discrepancy of the temperature and the gas pressure between the experimental data (Masuda *et al.*, 1999) against simulation results. In our simulation, the temperature is overestimated in the time period between zero and 6000 seconds. This is likely to be caused by the Joule-Thomson effect (Wang *et al*., 2018; Liu *et al*., 2019; Deng *et al*., 2020), which will absorb more heat when the gas is released from the hydrates and has not yet been considered in our model. For gas pressure, a local peak at about 3000s is not fully reflected, neither in Sun's (Sun *et al*., 2019) nor in our results. Through detailed investigation, it is found that a recent model proposed by Deng *et al.* (2020) captures this peak. Deng *et al*. suggested that this peak might be caused jointly by the Joule-Thomson effect, the compressibility coefficient of gas phase, the specific surface area related to absolute permeability and gas density governed by the Berthelot equation of state. The absolute derivations are also investigated in this work with respect to the temperature, gas pressure and volume of gas production. It can be inferred that the absolute derivations for these four variables are 0.192 K, 0.128 K, 0.047 MPa and 8.373 $\times 10^{-4}$ m^3 in Sun's results (Sun *et al*., 2019). In comparison, they are 0.182 K, 0.161 K, 0.031 MPa and 4.224 $\times 10^{-4}$ m^3 in our results respectively. Although the temperature at P3 in Sun's simulation (Sun *et al*., 2019) is more accurate, we are able to achieve closer fit with respect to the gas pressure and the volume of gas production. In Sun's model (2019), the impact of gas diffusion and vapor flux are not included. Our model in OGS-6 is capable of considering these but neglects the compressibility of solid / liquid and the variations of k^{π} / C^{π}. Despite of these differences, the developed OGS-6 model can still reproduce the NGH dissociation process and largely fit the experiment data.

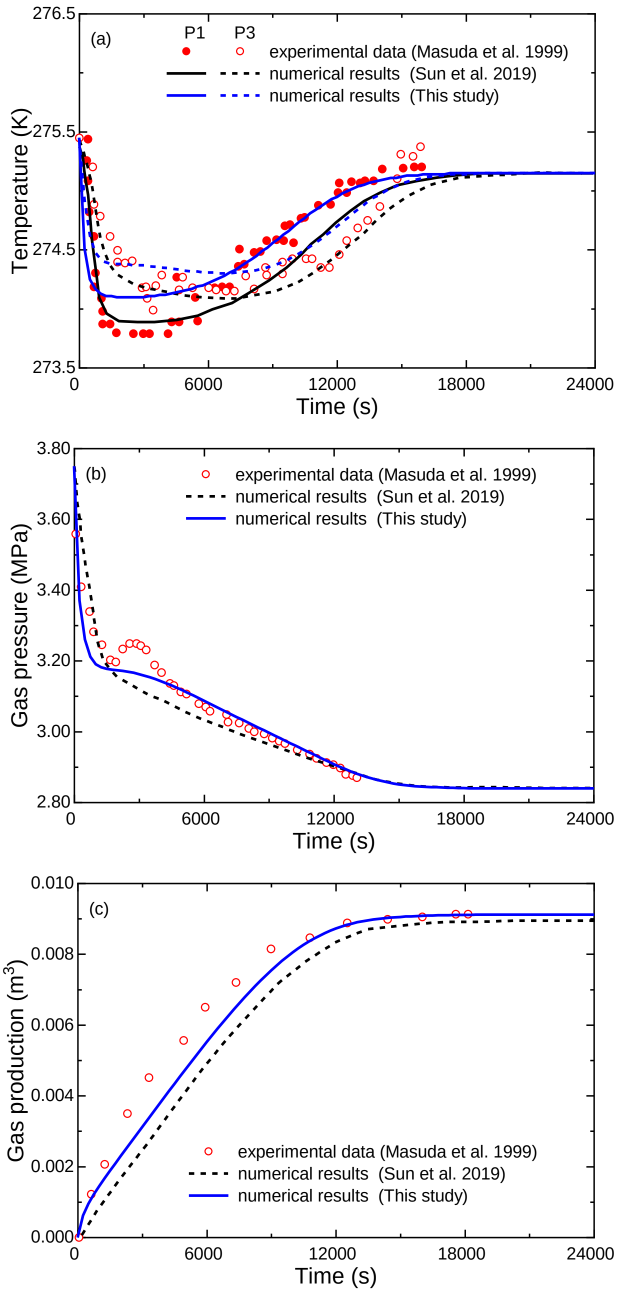

Fig. 6 Comparison of the evolutions of (a) temperature, (b) gas pressure, and (c) gas production volume simulated by the OGS-6 model, observed by Masuda *et al.* (1999) and solutions by Sun *et al.* (2019)

4 Numerical analyses of NGH exploitation by depressurization method

Based on the previously verified numerical model, we design a series of pilot-scale simulations in the section to discuss the scientific and engineering problems during the NGH exploitation in practice. The impacts of gravity effect on THCM coupled behavior is first investigated. For the engineering problem, the influence of vertical production wellbore length on gas production efficiency is also investigated.

4.1 Model configuration

The above scientific and engineering problems are investigated with a 2-dimensional pilot-scale numerical model. In reality, the thickness of hydrate-bearing sediments, *H*, varies from tens to hundreds of meters (Wang *et al*., 2017; Li *et al*., 2018; Ye *et al*., 2020). Here we offset the model thickness *H* value to 10 m. To make sure that the NGH dissociation process is not influence by the boundary effect, the radius *R* of the domain is set to a large value, i.e. 200 m here. This leads to an axisymmetric model domain as shown in Fig. 7, representing hydrate-bearing sediments. The top boundary is imposed with a constant load of 2.00 MPa to represent the lithostatic pressure. The parameters of soil, NGH, liquid and gas are the same with those listed in Tables 3. NGHs are exploited in this scenario by the depressurization method, in which the liquid and gas pressures are decreased from 3.75 MPa and 2.34 MPa to 2.84 MPa and 1.71 MPa respectively.

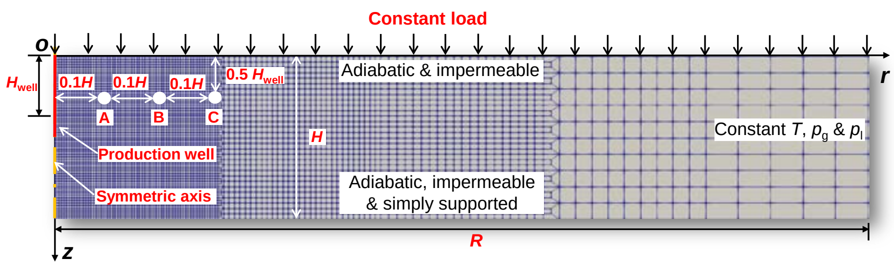

Fig. 7 Model domain, finite element mesh, initial and boundary conditions

To investigate the gravity effect, the length of the vertical production wellbore H_{well} is fixed to be 5 m, also recorded as $H_{\text{well}} = 0.50H$. The magnitude of the gravity vector $\mathbf{g}$ is noted as g. In the numerical model, $g = 9.8$ m/s^2 or 0 m/s^2 respectively, representing cases with or without the gravity effect. As for cases concerning the wellbore length, four scenarios are simulated, where $H_{\text{well}} = 0.25H$, $0.50H$, $0.75H$ and $1.00H$. To analyze the evolution of dissociation front, three points at the depth of $0.25H$ and at different radial distance from the wellbore, H_r, are monitored, where $H_r = 0.1H$, $0.2H$ and $0.3H$. In the following section, the z / H ratio is taken as a dimensionless number to indicate the spatial effect.

4.2 Gravity effect on THCM coupled behavior

To illustrate the impact of gravity effect, the simulated gas and NGH saturation are presented in its increment form in comparison to their initial distribution. Fig. 8 shows the simulated gas saturation increments at 1×10^6 s and 1×10^7 s, where the left side of the figure represents the results ignoring the gravity effect, and the right side considering it. It is found that gas saturation increases at the bottom of the wellbore (positive increment), and decreases sharply near the vertical wellbore (negative increment). At the moving front (Selim and Sloan, 1990; Yousif *et al*., 1991; Jin *et al*., 2018a), the dissociation front gradually expands over time from Fig. 8(a) to Fig. 8(b). The latter figure shows a larger area where the gas saturation increment value is positive. The hydrate-bearing sediments can be separated into the dissociated region and the undisturbed part by the dissociation front. Within this front, NGHs are completely dissociated. As the gas viscosity is far smaller than that of liquid, the dissipation of gas phase is also much faster than that of liquid migration. This means the dissociated natural gas moves faster in the gas phase and quickly enters the production wellbore when gravity is present. Meanwhile, the liquid phase will re-fill the influence area driven by the density effect. This causes a slight decline of gas saturation in the undisturbed region. It also creates great gradient near the NGH dissociation front. As a result, when considering the gravity effect, the gas saturation increments are generally lower, and the area of influenced region is also smaller. It can be inferred that this phenomenon will be enhanced with increasing thickness of hydrate-bearing sediments.

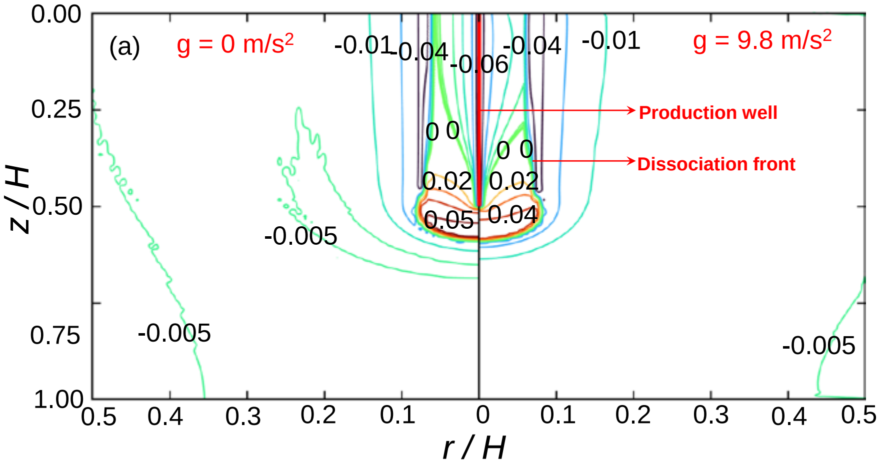

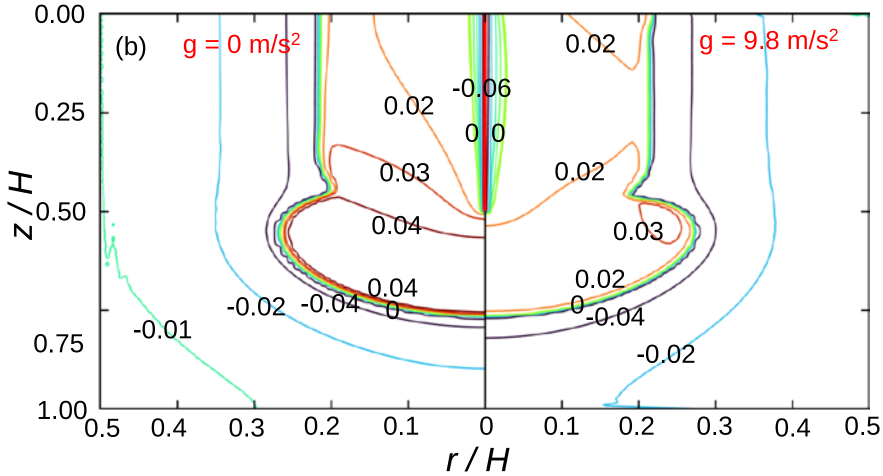

Fig. 8 Gravity effect on the distribution of gas saturation increments at: (a) 1×10^6 s; (b) 1×10^7 s

As depicted in Fig. 9(a), NGH saturation drops sharply around the vertical wellbore and decreases slightly at places far away from the dissociation front. This indicates that a small amount of NGHs will dissociate in the undisturbed region, which is caused by the aforementioned faster dissipation of gas phase compared to that of liquid phase and the induced gas pressure decrease. At the depth of $z / H = 0.4$, a local smaller radius of the dissociation front can be observed. This means that a large amount of NGHs dissociates at the bottom of the wellbore and less heat can be supplied from surrounding sediments at this depth. From Fig. 9(a) to Fig. 9(b), the dissociation front moves outwards over time, especially at the bottom of the wellbore, as the increasing time allows for thermal recharge from the surroundings. Compared to cases ignoring the gravity effect, a larger influence region can be observed. This is again facilitated by the faster gas dissipation driven by the gravity effect.

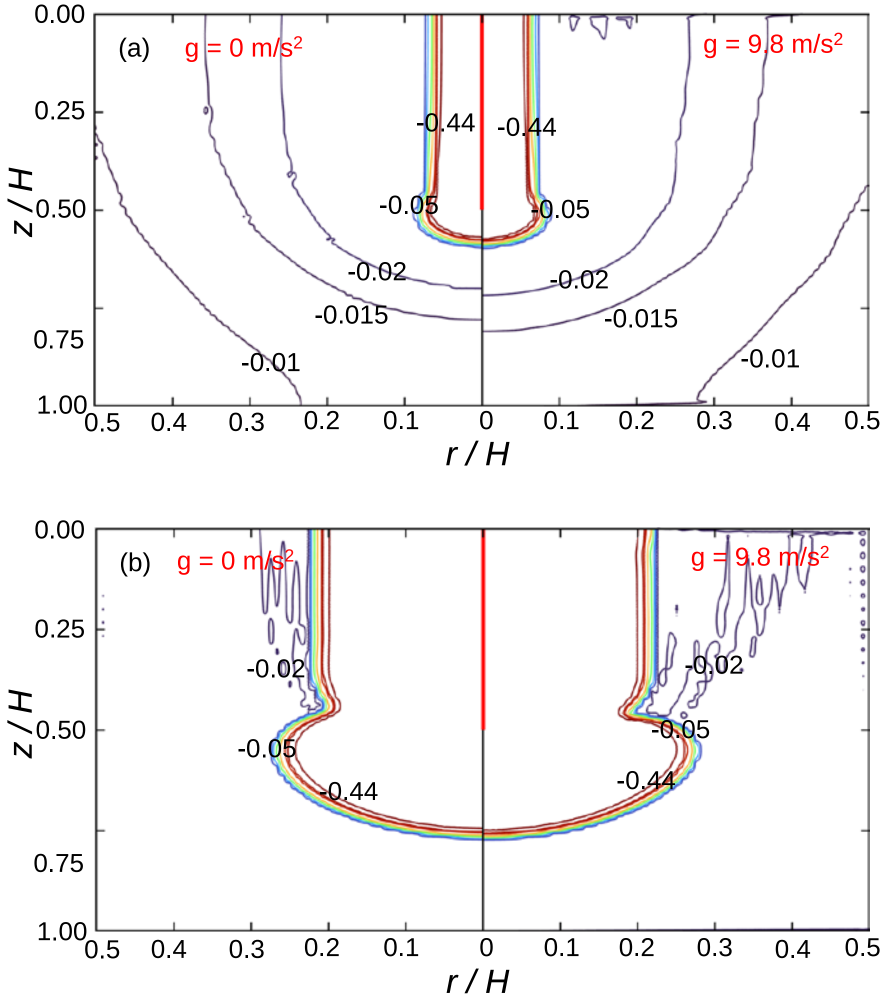

Fig. 9 Gravity effect on the distribution of NGH saturation increments at: (a) 1×10^6 s; (b) 1×10^7 s

In Fig. 10(a), it can be noticed that an apparent compression zone occurs near the vertical wellbore. This is caused by the great drop of pore gas / liquid pressure and the stiffness reduction of soil skeleton induced by NGH dissociation in Eq. (19). In Fig. 10(b) and 10(c), this behavior is further enhanced over time. Along with the propagation of the dissociation front over time, the vertical displacement curve in the radial direction gradually becomes smoother from Figs. 10(a) to 10(c). As illustrated in Figs. 10(a) and 10(b), when the gravity effect is on, the vertical displacement is evolving faster and further. This can be explained by the above-mentioned faster gas dissipation, thus showing the same trend as in the previous gas / NGH saturation distributions. After about four months (Fig. 10(c)), little difference in deformation can be observed. In summary, the gravity effect on THCM coupled behavior should be considered when the thickness of hydrate-bearing sediments is larger than tens of meters during NGH exploitations, especially for a short duration of hours and days. When the production wellbore is penetrating the entire depth of the hydrate-bearing reservoir, the gravity effect will have a minor impact on the pore gas dissipation and skeleton deformation. In comparison when $H_{\mathrm{well}} < H$, the gravity effect cannot be neglected. In the worst scenario, the spatial inhomogeneity of vertical displacement will push the hydrate-bearing sediments into plastic behavior, and may eventually cause hydrate related geotechnical hazards (Maslin *et al*., 2010; McConnell *et al*., 2012).

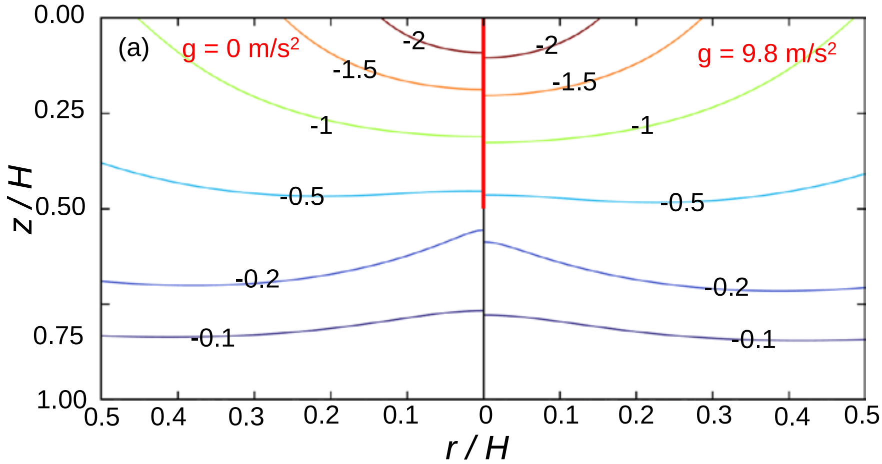

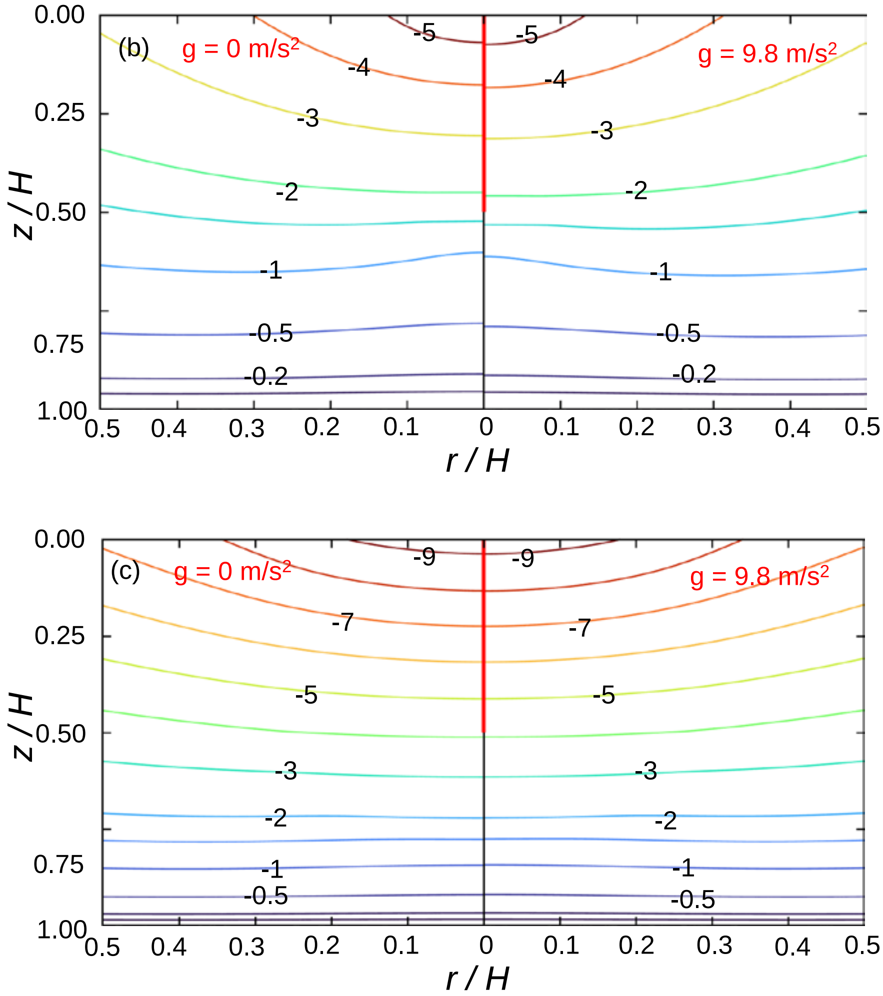

Fig. 10 Gravity effect on the distribution of vertical displacement (unit: mm) at: (a) 1×10^5 s; (b) 1×10^6 s; (c) 1×10^7 s

4.3 Effect of wellbore length on NGH exploitation

The impact of the wellbore length on the gas production during the NGH exploitation is discussed in this section. In detail, the evolutions of the gas / liquid / NGH saturation increment and gas production volume are simulated with different wellbore length to reservoir thickness ratio, and the results are shown below. Figure 11 depicts evolutions of these parameters at three different locations. Fig. 11(a) depicts the gas saturation increment at location A, B and C (see the white dot in Fig. 7). The gas saturation increment first drops slowly at the beginning but accelerate the decrease over time. After the start of NGH dissociation, the gas saturation increment sharply rises to a positive value. Meanwhile as shown in Fig. 11(b), liquid saturation increment always increases over time. Great changes happen at around 2×10^6 s when $H_r = 0.1H$, indicating that the dissociation front has arrived there. With the increase of H_{well}, the time of sharp decline in NGH saturation increment and the sudden rise of gas / liquid saturation increment is postponed. This is because a larger H_{well} means a smaller undisturbed region below the wellbore bottom, leading to less thermal recharge supporting the dissociation. When dissociation happens, it always leads to a sudden jump in liquid saturation, caused by the release of water from the NGHs. At the beginning stage, all parameters are controlled by gas-liquid migration process. After the NGH dissociation, generated gas / liquid mass will occupy the pore space, leading to the increase of gas / liquid saturation. Accordingly, dissipation and generation of gas / liquid alternatively dominate during the exploitation, which is reflected in the change of saturation curve.

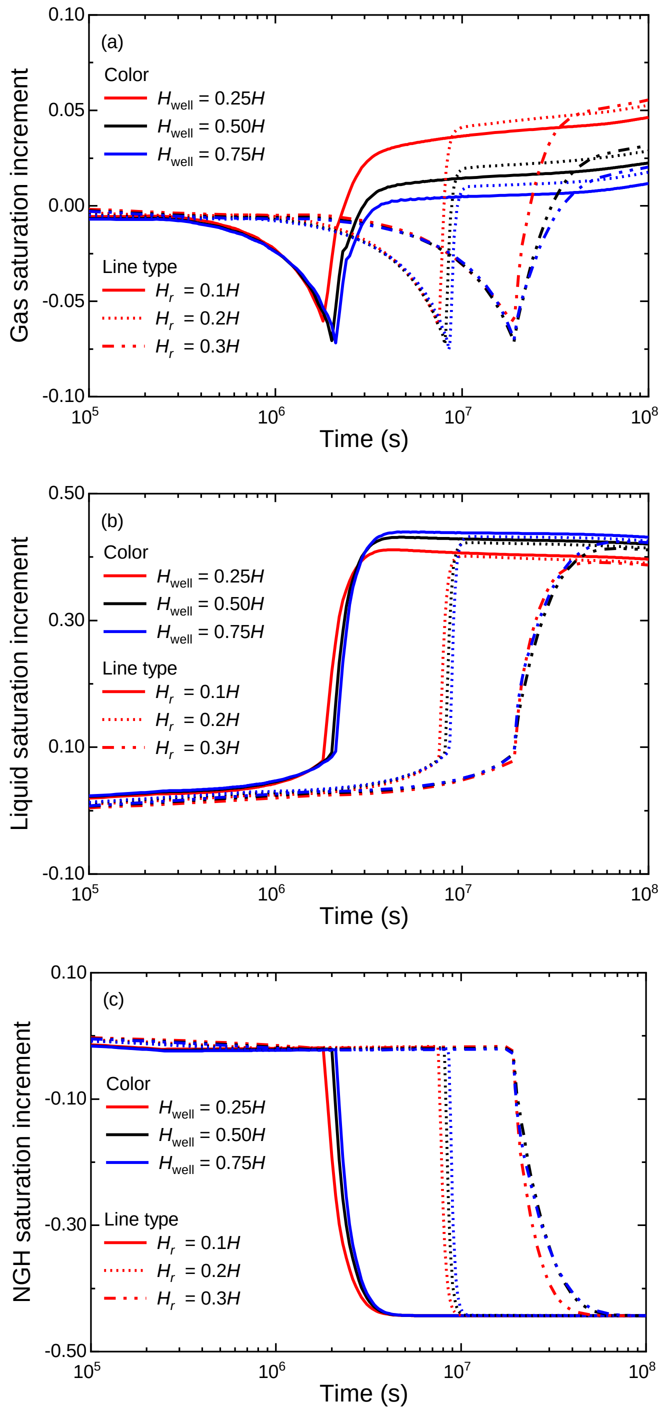

Fig. 11 Effect of wellbore length on evolutions of increments of: (a) gas saturation; (b) liquid saturation; (c) NGH saturation

As shown in Fig. 12, the volume of gas production rises with the increase of H_{well}, which always shows a sharp ascending tendency over a long period of time. This is because the large radius of the NGH reservoir will supply a continuous gas generation.

Obviously, the difference in gas production rate gradually reduces with the increase of H_{well}. Between $H_{well} = 0.75H$ and $H_{well} = 1.00H$, only little discrepancy can be observed. This suggests that the marginal production rate increase will happen when the wellbore length is increasing from $0.25H$ to $0.75H$, but not much more after H_{well} exceeds $0.75H$. In practical engineering, larger value of H_{well} indicates higher investment, meaning that reasonable value of H_{well} should be discussed when considering both efficiency and cost.

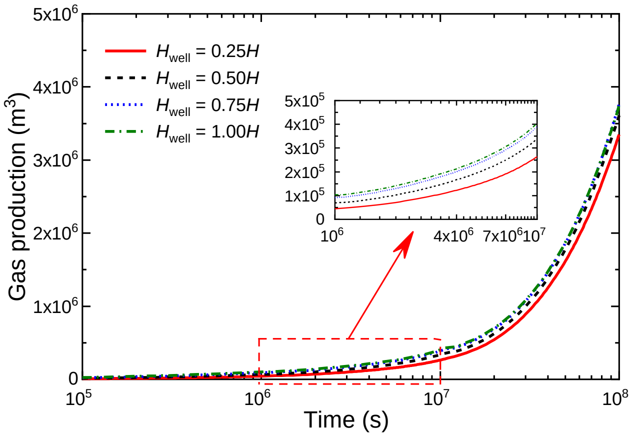

Fig. 12 Evolutions of gas production with different wellbore length

5 Conclusions

A new THCM coupled model has been developed in this work to investigate the behavior of hydrate-bearing sediments during the NGH dissociation, with explicit consideration of the gravity effect. The process of gas-liquid migration and NGH dissociation are implemented in the OGS-6 code. The numerical stability and efficiency of the NGH dissociation model is improved by expanding the source terms of governing equations and taking the first-order term of Taylor series. Furthermore, pre-calculation considering gravity have been carried out with explicit method, and then distributions of three variables (pressure, temperature and stresses) are set as initial conditions to analyze the impacts of gravity effect on THCM coupled behavior. The extended numerical model has been verified by two benchmarks, including one for THM coupled response of unsaturated soils and another for NGH dissociation. Main conclusions are summarized as follows:

(1) A dissociation front can be observed during the NGH exploitation, and the hydrate-bearing sediments can be separated into the dissociated region and the undisturbed part by this front. Generation of gas / liquid dominates at the dissociation front and gas-liquid migration predominates in the undisturbed region. As gas viscosity is much smaller than that of liquid phase, the dissipation of gas phase is much faster than that of pore liquid. This causes great increase of gas / liquid saturation at the front and slight decline of gas / NGH saturation in the undisturbed region.

(2) When the vertical production wellbore length $H_{\mathrm{well}} < H$, gas-liquid migration is accelerated by the gravity effect, which enhances the degree of gas saturation decline and the acceleration of liquid pressure dissipation compared to that without it. This leads to the faster NGH dissociation, the larger soil deformation and a larger influence region in a short period of time. Gravity effect on gas-liquid migration and NGH dissociation will be enhanced by the increase of hydrate-bearing sediments thickness and cannot be ignored when the thickness exceeds tens of meters.

(3) Dissipation and generation of gas / liquid alternatively dominate during the NGH exploitation. That is to say, gas saturation decreases in the early stage and increase

subsequently, while liquid saturation increases all the time. When dissociation happens, it always leads to a sudden jump in gas / liquid saturation, caused by the release of gas / water from the NGHs. Obvious difference of gas production appears with the increase of vertical wellbore length H_{well} when $H_{\mathrm{well}} < 0.75H$ while negligible difference occurs when $H_{\mathrm{well}} > 0.75H$.

Acknowledgement

The authors acknowledge the funding from the National Natural Science Foundation of China (Nos. 51988101, 52127815 and 52078458), and the Zhejiang Provincial Natural Science Foundation of China (No. LCD19E090001). The first author is grateful to all the members of the OpenGeoSys team, especially Prof. Olaf Kolditz and Prof. Thomas Nagel for supporting his research stay in Germany.

Appendix I

The mass equation of soil skeleton is:

$$\frac{\mathrm{d_s}}{\mathrm{d}t}\left(\rho^{\mathrm{s}}(1-\varphi)\right) + \rho^{\mathrm{s}}(1-\varphi)\nabla\cdot\mathbf{v}^{\mathrm{s}} = 0 \tag{I-1}$$

where ρ^{s} is the solid phase density, $\mathbf{v}^{\mathrm{s}}$ is the velocity of soil skeleton and $\frac{\mathrm{d_s}}{\mathrm{d}t}$ denotes the material time derivative following the solid skeleton. Eq. (I-1) can be expressed as:

$$\frac{\mathrm{d_s}\varphi}{\mathrm{d}t} = \frac{1-\varphi}{\rho^{\mathrm{s}}}\frac{\mathrm{d_s}\rho^{\mathrm{s}}}{\mathrm{d}t} + (1-\varphi)\nabla\cdot\mathbf{v}^{\mathrm{s}} \tag{I-2a}$$

$$\frac{1}{\rho^{\mathrm{s}}}\frac{\mathrm{d_s}\rho^{\mathrm{s}}}{\mathrm{d}t} = -\beta_{\mathrm{s}}\frac{\mathrm{d_s}T}{\mathrm{d}t} \tag{I-2b}$$

$$\nabla\cdot\mathbf{v}^{\mathrm{s}} = \nabla\cdot\frac{\mathrm{d_s}\mathbf{u}}{\mathrm{d}t} \tag{I-2c}$$

Combining with Eqs. (I-2b) and (I-2c) considering the assumption of incompressible solid phase, Eq. (I-2) can be transformed to:

$$\frac{\mathrm{d_s}\boldsymbol{\varphi}}{\mathrm{d}t} = -(1-\varphi)\beta_\mathrm{s}\frac{\mathrm{d_s}T}{\mathrm{d}t} + (1-\varphi)\nabla\cdot\frac{\mathrm{d_s}\mathbf{u}}{\mathrm{d}t} \tag{I-3}$$

Analogous to what has been used in (I-2b), the volumetric thermal expansion coefficient of water and NGHs are defined as:

$$\frac{1}{\rho^\mathrm{w}}\frac{\partial\rho^\mathrm{w}}{\partial T} = -\beta_\mathrm{w} \tag{I-4a}$$

$$\frac{1}{\rho^\mathrm{h}}\frac{\partial\rho^\mathrm{h}}{\partial T} = -\beta_\mathrm{h} \tag{I-4b}$$

Appendix II

The matrices in Eq. (28) are defined as follows:

$$\mathbf{M}_\mathrm{gg} = \int \mathbf{N}_\mathrm{g}^\mathrm{T}\left(-\varphi\rho_\mathrm{a}^\mathrm{g}\frac{\partial S^\mathrm{l}}{\partial p^\mathrm{g}} - \varphi S^\mathrm{g}\frac{M_\mathrm{a}}{RT}\frac{\partial p_\mathrm{w}^\mathrm{g}}{\partial p^\mathrm{g}} + \varphi S^\mathrm{g}\frac{M_\mathrm{a}}{RT}\right)\mathbf{N}_\mathrm{g}\,\mathrm{d}\Omega \tag{II-1}$$

$$\mathbf{M}_\mathrm{gl} = \int \mathbf{N}_\mathrm{g}^\mathrm{T}\left(-\varphi\rho_\mathrm{a}^\mathrm{g}\frac{\partial S^\mathrm{l}}{\partial p^\mathrm{l}} - \varphi S^\mathrm{g}\frac{M_\mathrm{a}}{RT}\frac{\partial p_\mathrm{w}^\mathrm{g}}{\partial p^\mathrm{l}}\right)\mathbf{N}_\mathrm{l}\,\mathrm{d}\Omega \tag{II-2}$$

$$\mathbf{M}_\mathrm{gT} = \int \mathbf{N}_\mathrm{g}^\mathrm{T}\left(-(1-\varphi)\rho_\mathrm{a}^\mathrm{g}S^\mathrm{g}\beta_\mathrm{s} - \varphi\rho_\mathrm{a}^\mathrm{g}\frac{\partial S^\mathrm{h}}{\partial T} - \varphi S^\mathrm{g}\frac{M_\mathrm{a}}{RT}\left(\frac{p^\mathrm{g}}{T} + \frac{\partial p_\mathrm{w}^\mathrm{g}}{\partial T} - \frac{p_\mathrm{w}^\mathrm{g}}{T}\right)\right)\mathbf{N}_T\,\mathrm{d}\Omega \tag{II-3}$$

$$\mathbf{M}_\mathrm{gu} = \int \mathbf{N}_\mathrm{g}^\mathrm{T}\left(\rho_\mathrm{a}^\mathrm{g}S^\mathrm{g} - \varphi\rho_\mathrm{a}^\mathrm{g}\frac{\partial S^\mathrm{h}}{\partial(\nabla\mathbf{u})}\right)\nabla\mathbf{N}_\mathbf{u}\,\mathrm{d}\Omega \tag{II-4}$$

$$\mathbf{K}_\mathrm{gg} = \int \nabla\mathbf{N}_\mathrm{g}^\mathrm{T}\left(\rho_\mathrm{a}^\mathrm{g}\frac{\mathbf{K}k_\mathrm{rel}^\mathrm{g}}{\mu^\mathrm{g}} + \rho^\mathrm{g}\frac{M_\mathrm{a}M_\mathrm{w}}{\left(M_\mathrm{g}\right)^2}\mathbf{D}_\mathrm{a}^\mathrm{g}\left(-\frac{1}{p^\mathrm{g}}\frac{\partial p_\mathrm{w}^\mathrm{g}}{\partial p^\mathrm{g}} + \frac{p_\mathrm{w}^\mathrm{g}}{(p^\mathrm{g})^2}\right)\right)\nabla\mathbf{N}_\mathrm{g}\,\mathrm{d}\Omega + \int \mathbf{N}_\mathrm{g}^\mathrm{T}\left(\left(\frac{\rho_\mathrm{a}^\mathrm{g}M_\mathrm{h}}{\rho^\mathrm{h}} - \right.\right.$$

$$\left.\left.M_\mathrm{g}\right)\frac{\partial R_\mathrm{r}}{\partial p^\mathrm{g}}\right)\mathbf{N}_\mathrm{g}\,\mathrm{d}\Omega \tag{II-5}$$

$$\mathbf{K}_\mathrm{gl} = \int \nabla\mathbf{N}_\mathrm{g}^\mathrm{T}\left(\rho^\mathrm{g}\frac{M_\mathrm{a}M_\mathrm{w}}{\left(M_\mathrm{g}\right)^2}\mathbf{D}_\mathrm{a}^\mathrm{g}\left(-\frac{1}{p^\mathrm{g}}\frac{\partial p_\mathrm{w}^\mathrm{g}}{\partial p^\mathrm{l}}\right)\right)\nabla\mathbf{N}_\mathrm{l}\,\mathrm{d}\Omega \tag{II-6}$$

$$\mathbf{K}_\mathrm{gT} = \int \nabla\mathbf{N}_\mathrm{g}^\mathrm{T}\left(\rho^\mathrm{g}\frac{M_\mathrm{a}M_\mathrm{w}}{\left(M_\mathrm{g}\right)^2}\mathbf{D}_\mathrm{a}^\mathrm{g}\left(-\frac{1}{p^\mathrm{g}}\frac{\partial p_\mathrm{w}^\mathrm{g}}{\partial T}\right)\right)\nabla\mathbf{N}_T\,\mathrm{d}\Omega + \int \mathbf{N}_\mathrm{g}^\mathrm{T}\left(\left(\frac{\rho_\mathrm{a}^\mathrm{g}M_\mathrm{h}}{\rho^\mathrm{h}} - M_\mathrm{g}\right)\frac{\partial R_\mathrm{r}}{\partial T}\right)\mathbf{N}_T\,\mathrm{d}\Omega \tag{II-7}$$

$$\mathbf{f}_\mathrm{g} = \int \nabla\mathbf{N}_\mathrm{g}^\mathrm{T}\left(\rho_\mathrm{a}^\mathrm{g}\frac{\mathbf{K}k_\mathrm{rel}^\mathrm{g}}{\mu^\mathrm{g}}\rho^\mathrm{g}\mathbf{g}\right)\mathrm{d}\Omega + \int \mathbf{N}_\mathrm{g}^\mathrm{T}\left(\left(M_\mathrm{g} - \frac{\rho_\mathrm{a}^\mathrm{g}M_\mathrm{h}}{\rho^\mathrm{h}}\right)\left(R_\mathrm{r}\left(\mathbf{X}_0, S_t^\mathrm{h}\right) - \frac{\partial R_\mathrm{r}\left(\mathbf{X}_0, S_t^\mathrm{h}\right)}{\partial\mathbf{X}}\cdot\mathbf{X}_0\right)\right)\mathrm{d}\Omega -$$

$$\int \mathbf{N}_{\mathrm{g}}^{\mathrm{T}}\left(q^{\mathrm{a}}+q^{\mathrm{ga}}\right) \mathrm{d}\Gamma \tag{II-8}$$

$$\mathbf{M}_{\mathrm{lg}}=\int \mathbf{N}_{\mathrm{l}}^{\mathrm{T}}\left(\varphi\left(\rho_{\mathrm{w}}^{\mathrm{l}}-\rho_{\mathrm{w}}^{\mathrm{g}}\right) \frac{\partial S^{\mathrm{l}}}{\partial p^{\mathrm{g}}}+\varphi S^{\mathrm{g}} \frac{M_{\mathrm{w}}}{R T} \frac{\partial p_{\mathrm{w}}^{\mathrm{g}}}{\partial p^{\mathrm{g}}}\right) \mathbf{N}_{\mathrm{g}}\, \mathrm{d}\Omega \tag{II-9}$$

$$\mathbf{M}_{\mathrm{ll}}=\int \mathbf{N}_{\mathrm{l}}^{\mathrm{T}}\left(\varphi\left(\rho_{\mathrm{w}}^{\mathrm{l}}-\rho_{\mathrm{w}}^{\mathrm{g}}\right) \frac{\partial S^{\mathrm{l}}}{\partial p^{\mathrm{l}}}+\varphi S^{\mathrm{g}} \frac{M_{\mathrm{w}}}{R T} \frac{\partial p_{\mathrm{w}}^{\mathrm{g}}}{\partial p^{\mathrm{l}}}\right) \mathbf{N}_{\mathrm{l}}\, \mathrm{d}\Omega \tag{II-10}$$

$$\mathbf{M}_{\mathrm{lT}}=\int \mathbf{N}_{\mathrm{l}}^{\mathrm{T}}\left(-(1-\varphi)\left(\rho_{\mathrm{w}}^{\mathrm{l}} S^{\mathrm{l}}+\rho_{\mathrm{w}}^{\mathrm{g}} S^{\mathrm{g}}\right) \beta_{\mathrm{s}}-\varphi \rho_{\mathrm{w}}^{\mathrm{l}} S^{\mathrm{l}} \beta_{\mathrm{w}}-\varphi \rho_{\mathrm{w}}^{\mathrm{g}} \frac{\partial S^{\mathrm{h}}}{\partial T}+\varphi S^{\mathrm{g}} \frac{M_{\mathrm{w}}}{R T}\left(\frac{\partial p_{\mathrm{w}}^{\mathrm{g}}}{\partial T}-\frac{p_{\mathrm{w}}^{\mathrm{g}}}{T}\right)\right) \mathbf{N}_{T}\, \mathrm{d}\Omega \tag{II-11}$$

$$\mathbf{M}_{\mathrm{lu}}=\int \mathbf{N}_{\mathrm{l}}^{\mathrm{T}}\left(\left(\rho_{\mathrm{w}}^{\mathrm{l}} S^{\mathrm{l}}+\rho_{\mathrm{w}}^{\mathrm{g}} S^{\mathrm{g}}\right)-\varphi \rho_{\mathrm{w}}^{\mathrm{g}} \frac{\partial S^{\mathrm{h}}}{\partial(\nabla \mathbf{u})}\right) \nabla \mathbf{N}_{\mathbf{u}}\, \mathrm{d}\Omega \tag{II-12}$$

$$\mathbf{K}_{\mathrm{lg}}=\int \nabla \mathbf{N}_{\mathrm{l}}^{\mathrm{T}}\left(\rho_{\mathrm{w}}^{\mathrm{g}} \frac{\mathbf{K} k_{\mathrm{rel}}^{\mathrm{g}}}{\mu^{\mathrm{g}}}+\rho^{\mathrm{g}} \frac{M_{\mathrm{a}} M_{\mathrm{w}}}{\left(M_{\mathrm{g}}\right)^{2}} \mathbf{D}_{\mathrm{a}}^{\mathrm{g}}\left(\frac{1}{p^{\mathrm{g}}} \frac{\partial p_{\mathrm{w}}^{\mathrm{g}}}{\partial p^{\mathrm{g}}}-\frac{p_{\mathrm{w}}^{\mathrm{g}}}{\left(p^{\mathrm{g}}\right)^{2}}\right)\right) \nabla \mathbf{N}_{\mathrm{g}}\, \mathrm{d}\Omega+\int \mathbf{N}_{\mathrm{l}}^{\mathrm{T}}\left(\left(\frac{\rho_{\mathrm{w}}^{\mathrm{g}} M_{\mathrm{h}}}{\rho^{\mathrm{h}}}-N_{\mathrm{h}} M_{\mathrm{w}}\right) \frac{\partial R_{\mathrm{r}}}{\partial p^{\mathrm{g}}}\right) \mathbf{N}_{\mathrm{g}}\, \mathrm{d}\Omega \tag{II-13}$$

$$\mathbf{K}_{\mathrm{ll}}=\int \nabla \mathbf{N}_{\mathrm{l}}^{\mathrm{T}}\left(\rho_{\mathrm{w}}^{\mathrm{l}} \frac{\mathbf{K} k_{\mathrm{rel}}^{\mathrm{l}}}{\mu^{\mathrm{l}}}+\rho^{\mathrm{g}} \frac{M_{\mathrm{a}} M_{\mathrm{w}}}{\left(M_{\mathrm{g}}\right)^{2}} \mathbf{D}_{\mathrm{a}}^{\mathrm{g}}\left(\frac{1}{p^{\mathrm{g}}} \frac{\partial p_{\mathrm{w}}^{\mathrm{g}}}{\partial p^{\mathrm{l}}}\right)\right) \nabla \mathbf{N}_{\mathrm{l}}\, \mathrm{d}\Omega \tag{II-14}$$

$$\mathbf{K}_{\mathrm{lT}}=\int \nabla \mathbf{N}_{\mathrm{l}}^{\mathrm{T}}\left(\rho^{\mathrm{g}} \frac{M_{\mathrm{a}} M_{\mathrm{w}}}{\left(M_{\mathrm{g}}\right)^{2}} \mathbf{D}_{\mathrm{a}}^{\mathrm{g}}\left(\frac{1}{p^{\mathrm{g}}} \frac{\partial p_{\mathrm{w}}^{\mathrm{g}}}{\partial T}\right)\right) \nabla \mathbf{N}_{T}\, \mathrm{d}\Omega+\int \mathbf{N}_{\mathrm{l}}^{\mathrm{T}}\left(\left(\frac{\rho_{\mathrm{w}}^{\mathrm{g}} M_{\mathrm{h}}}{\rho^{\mathrm{h}}}-N_{\mathrm{h}} M_{\mathrm{w}}\right) \frac{\partial R_{\mathrm{r}}}{\partial T}\right) \mathbf{N}_{T}\, \mathrm{d}\Omega$$

(II-15)

$$\mathbf{f}_{\mathrm{l}}=\int \nabla \mathbf{N}_{\mathrm{l}}^{\mathrm{T}}\left(\rho_{\mathrm{w}}^{\mathrm{l}} \frac{\mathbf{K} k_{\mathrm{rel}}^{\mathrm{l}}}{\mu^{\mathrm{l}}} \rho_{\mathrm{w}}^{\mathrm{l}} \mathbf{g}+\rho_{\mathrm{w}}^{\mathrm{g}} \frac{\mathbf{K} k_{\mathrm{rel}}^{\mathrm{g}}}{\mu^{\mathrm{g}}} \rho^{\mathrm{g}} \mathbf{g}\right) \mathrm{d}\Omega+\int \mathbf{N}_{\mathrm{l}}^{\mathrm{T}}\left(\left(N_{\mathrm{h}} M_{\mathrm{w}}-\frac{\rho_{\mathrm{w}}^{\mathrm{g}} M_{\mathrm{h}}}{\rho^{\mathrm{h}}}\right)\left(R_{\mathrm{r}}\left(\mathbf{X}_{0}, S_{t}^{\mathrm{h}}\right)-\frac{\partial R_{\mathrm{r}}\left(\mathbf{X}_{0}, S_{t}^{\mathrm{h}}\right)}{\partial \mathbf{X}} \cdot \mathbf{X}_{0}\right)\right) \mathrm{d}\Omega-\int \mathbf{N}_{\mathrm{l}}^{\mathrm{T}}\left(q^{\mathrm{l}}+q^{\mathrm{gw}}\right) \mathrm{d}\Gamma \tag{II-16}$$

$$\mathbf{M}_{\mathrm{TT}}=\int \mathbf{N}_{\mathrm{T}}^{\mathrm{T}}(\rho C) \mathbf{N}_{T}\, \mathrm{d}\Omega \tag{II-17}$$

$$\mathbf{K}_{\mathrm{Tg}}=\int \mathbf{N}_{T}^{\mathrm{T}}\left(-C^{\mathrm{g}} \rho^{\mathrm{g}} \frac{\mathbf{K} k_{\mathrm{rel}}^{\mathrm{g}}}{\mu^{\mathrm{g}}}\right) \nabla \mathbf{N}_{\mathrm{g}} \nabla T\, \mathrm{d}\Omega+\int \mathbf{N}_{T}^{\mathrm{T}}\left(\Delta H M_{\mathrm{h}} \frac{\partial R_{\mathrm{r}}}{\partial p^{\mathrm{g}}}\right) \mathbf{N}_{\mathrm{g}}\, \mathrm{d}\Omega \tag{II-18}$$

$$\mathbf{K}_{\mathrm{Tl}}=\int \mathbf{N}_{T}^{\mathrm{T}}\left(-C^{\mathrm{l}} \rho^{\mathrm{l}} \frac{\mathbf{K} k_{\mathrm{rel}}^{\mathrm{l}}}{\mu^{\mathrm{l}}}\right) \nabla \mathbf{N}_{\mathrm{l}} \nabla T\, \mathrm{d}\Omega \tag{II-19}$$

$$\mathbf{K}_{\mathrm{TT}}=\int \nabla \mathbf{N}_{T}^{\mathrm{T}}\left(\mathbf{k}_{T}\right) \nabla \mathbf{N}_{T}\, \mathrm{d}\Omega+\int \nabla \mathbf{N}_{T}^{\mathrm{T}}\left(C^{\mathrm{l}} \rho^{\mathrm{l}} \mathbf{v}^{\mathrm{l}}+C^{\mathrm{g}} \rho^{\mathrm{g}} \mathbf{v}^{\mathrm{g}}\right) \mathbf{N}_{T}\, \mathrm{d}\Omega+\int \mathbf{N}_{\mathrm{g}}^{\mathrm{T}}\left(\Delta H M_{\mathrm{h}} \frac{\partial R_{\mathrm{r}}}{\partial T}\right) \mathbf{N}_{T}\, \mathrm{d}\Omega$$

(II-20)

$$\mathbf{f}_{\mathrm{T}} = \int \mathbf{N}_T^{\mathrm{T}} \left(C^{\mathrm{l}} \rho_{\mathrm{w}}^{\mathrm{l}} \frac{\mathbf{K} k_{\mathrm{rel}}^{\mathrm{l}}}{\mu^{\mathrm{l}}} \rho_{\mathrm{w}}^{\mathrm{l}} \mathbf{g} + C^{\mathrm{g}} \rho^{\mathrm{g}} \frac{\mathbf{K} k_{\mathrm{rel}}^{\mathrm{g}}}{\mu^{\mathrm{g}}} \rho^{\mathrm{g}} \mathbf{g} \right) \nabla T \, \mathrm{d}\Omega + \int \mathbf{N}_T^{\mathrm{T}} \left(-\Delta H M_{\mathrm{h}} \left(R_{\mathrm{r}}\left(\mathbf{X}_0, S_t^{\mathrm{h}}\right) - \frac{\partial R_{\mathrm{r}}\left(\mathbf{X}_0, S_t^{\mathrm{h}}\right)}{\partial \mathbf{X}} \cdot \mathbf{X}_0 \right) \right) \mathrm{d}\Omega - \int \mathbf{N}_T^{\mathrm{T}} \left(q^{\mathrm{E}} + \alpha_{\mathrm{c}} (T_{\mathrm{c}} - T) \right) \mathrm{d}\Gamma \qquad \text{(II-21)}$$

$$\mathbf{K}_{\mathrm{ug}} = \int \nabla \mathbf{N}_{\mathbf{u}}^{\mathrm{T}} \left(-\frac{S^{\mathrm{g}}}{S^{\mathrm{l}} + S^{\mathrm{g}}} \right) \mathbf{1} \mathbf{N}_{\mathrm{g}} \mathrm{d}\Omega \qquad \text{(II-22)}$$

$$\mathbf{K}_{\mathrm{ul}} = \int \nabla \mathbf{N}_{\mathbf{u}}^{\mathrm{T}} \left(-\frac{S^{\mathrm{l}}}{S^{\mathrm{l}} + S^{\mathrm{g}}} \right) \mathbf{1} \mathbf{N}_{\mathrm{l}} \mathrm{d}\Omega \qquad \text{(II-23)}$$

$$\mathbf{K}_{\mathrm{uT}} = \int \nabla \mathbf{N}_{\mathbf{u}}^{\mathrm{T}} \left(\mathbf{D}^{\mathbf{e}} \mathbf{:1} \right) \alpha^{\mathrm{s}} \mathbf{N}_T \mathrm{d}\Omega \qquad \text{(II-24)}$$

$$\mathbf{K}_{\mathrm{uu}} = \int \nabla \mathbf{N}_{\mathbf{u}}^{\mathrm{T}} \mathbf{D}^{\mathbf{e}} \, \nabla \mathbf{N}_{\mathbf{u}} \mathrm{d}\Omega \qquad \text{(II-25)}$$

$$\mathbf{f}_{\mathrm{u}} = \int \mathbf{N}_{\mathbf{u}}^{\mathrm{T}} \left(\rho^{\mathrm{s}} (1 - \varphi) + \rho^{\mathrm{l}} S^{\mathrm{l}} \varphi + \rho^{\mathrm{g}} S^{\mathrm{g}} \varphi + \rho^{\mathrm{h}} S^{\mathrm{h}} \varphi \right) \mathbf{g} \mathrm{d}\Omega + \int \mathbf{N}_{\mathbf{u}}^{\mathrm{T}} \bar{\mathbf{t}} \, \mathrm{d}\Gamma \qquad \text{(II-26)}$$

References

[1] Bai Y, Yang H, Du Y *et al*. (2013). The sensitivity analysis of scaling criteria in gas hydrate reservoir physical simulation. Energy Conversion and Management. 67:138-144.

[2] Bilke L, Flemisch B, Kalbacher T *et al*. (2019). Development of open-source porous media simulators: principles and experiences. Transport in Porous Media. 130(1): 337-361.

[3] Boswell R, Schoderbek D, Collett T S *et al*. (2017). The Ignik Sikumi field experiment, Alaska North Slope: design, operations, and implications for CO_2-CH_4 exchange in gas hydrate reservoirs. Energy and Fuels. 31(1): 140-153.

[4] COMSOL. (2017). Reference Manual Version 5.3. COMSOL Corporation, Stockholm, Sweden.

[5] Corey A T. (1954). The interrelation between gas and oil relative permeabilities. Producers Monthly. 19(1): 38-41.

[6] Chen X J, Lu H L, Gu L J *et al*. (2022). Preliminary evaluation of the economic potential of the technologies for gas hydrate exploitation. Energy. 243: 123007.

[7] De La Fuente M, Vaunat J, Marín-Moreno H. (2020). A densification mechanism to model the mechanical effect of methane hydrates in sandy sediments. International Journal for

Numerical and Analytical Methods in Geomechanics. 44(6): 782-802.

[8] Deng X J, Feng J W, Pan S W *et al*. (2020). An improved model for the migration of fluids caused by hydrate dissociation in porous media. Journal of Petroleum Science and Engineering. 188: 106876.

[9] Gupta S, Helmig R and Wohlmuth B. (2015). Non-isothermal, multi-phase, multi-component flows through deformable methane hydrate reservoirs. Computational Geosciences. 19(5): 1063-1088.

[10] Hardwick J S and Mathias S A. (2018). Masuda's sandstone core hydrate dissociation experiment revisited. Chemical Engineering Science. 175: 98-109.

[11] Jin G, Lei H, Xu T *et al*. (2018a). Simulated geomechanical responses to marine methane hydrate recovery using horizontal wells in the Shenhu area, South China Sea. Marine and Petroleum Geology. 92: 424-436.

[12] Jin Y, Li S, Yang D *et al*. (2018b). Determination of dissociation front and operational optimization for hydrate development by combining depressurization and hot brine stimulation. Journal of Natural Gas Science and Engineering. 50: 215-230.

[13] Kim A R, Kim J T, Cho G C *et al*. (2018). Methane production from marine gas hydrate deposits in Korea: Thermal-hydraulic-mechanical simulation on production wellbore stability. Journal of Geophysical Research: Solid Earth. 123(11): 9555-9569.

[14] Kim H C, Bishnoi P R, Heidemann R A *et al*. (1987). Kinetics of methane hydrate decomposition. Chemical Engineering Science. 42(7): 1645-1653.

[15] Kimoto S, Oka F, Fushita T *et al*. (2007). A chemo-thermo-mechanically coupled numerical simulation of the subsurface ground deformations due to methane hydrate dissociation. Computers and Geotechnics. 34(4): 216-228.

[16] Kimoto S, Oka F and Fushita T. (2010). A chemo–thermo–mechanically coupled analysis of ground deformation induced by gas hydrate dissociation. International Journal of Mechanical Sciences. 52(2): 365-376.

[17] Klar A, Uchida S, Soga K *et al*. (2013). Explicitly coupled thermal flow mechanical formulation for gas-hydrate sediments. Spe Journal. 18(2): 196-206.

[18] Kleinberg R L, Flaum C, Griffin D D *et al*. (2003). Deep sea NMR: Methane hydrate growth habit in porous media and its relationship to hydraulic permeability, deposit accumulation, and submarine slope stability. Journal of Geophysical Research: Solid Earth. 108(B10): 2508.

[19] Kolditz O, Bauer S, Bilke L *et al*. (2012). OpenGeoSys: an open-source initiative for numerical simulation of thermo-hydro-mechanical/chemical (THM/C) processes in porous media. Environmental Earth Sciences. 67(2): 589-599.

[20] Kolditz O, Görke U-J, Shao H B *et al*. (2016). Thermo-hydro-mechanical chemical processesin fractured porous media: modelling and benchmarking. 1-314. Berlin: Springer.

[21] Konno Y, Fujii T, Sato A *et al*. (2017). Key findings of the world's first offshore methane hydrate production test off the coast of Japan: Toward future commercial production. Energy and Fuels. 31(3): 2607-2616.

[22] Kowalsky M B and Moridis G J. (2007) Comparison of kinetic and equilibrium reaction models in simulating gas hydrate behavior in porous media. Energy Conversion and Management. 48(6):1850-1863.

[23] Kumar A, Maini B, Bishnoi P R *et al*. (2010). Experimental determination of permeability in the presence of hydrates and its effect on the dissociation characteristics of gas hydrates in porous media. Journal of Petroleum Science and Engineering. 70(1-2): 114-122.

[24] Kvenvolden K A. (1988). Methane hydrate-a major reservoir of carbon in the shallow geosphere? Chemical Geology. 71(1-3): 41-51.

[25] Kwon T H, Oh T M, Choo Y W *et al*. (2013). Geomechanical and thermal responses of hydrate-bearing sediments subjected to thermal stimulation: Physical modeling using a geotechnical centrifuge. Energy and Fuels. 27(8): 4507-4522.

[26] Lehmann C, Kolditz O and Nagel T. (2018). The FEM Simulation Software OpenGeoSys 6. InModels of Thermochemical Heat Storage. 29-48. Springer: Cham.

[27] Li B, Li X S and Li G. (2014). Kinetic studies of methane hydrate formation in porous media based on experiments in a pilot-scale hydrate simulator and a new model. Chemical Engineering Science. 105: 220-230.

[28] Li J F, Ye J L, Qin X W *et al*. (2018). The first offshore natural gas hydrate production test in South China Sea. China Geology. 1(1): 5-16.

[29] Liang H F, Song Y C and Chen Y J. (2010). Numerical simulation for laboratory-scale methane hydrate dissociation by depressurization. Energy Conversion and Management. 51(10):1883-1890.

[30] Liu L, Lu X, Zhang X *et al*. (2017). Numerical simulations for analyzing deformation characteristics of hydrate-bearing sediments during depressurization. Advances in Geo-Energy Research. 1(3): 135-147.

[31] Liu Z Y, Yang M J, Liu Y *et al*. (2019). Analyzing the Joule-Thomson effect on wellbore in methane hydrate depressurization with different back pressure. Energy Procedia. 158: 5390-5395.

[32] Makogon Y F, Holditch S A and Makogon T Y. (2007). Natural gas-hydrates-A potential energy source for the 21st Century. Journal of Petroleum Science and Engineering. 56(1-3): 14-31.

[33] Maslin M, Owen M, Betts R *et al*. (2010). Gas hydrates: past and future geohazard? Philosophical Transactions of the Royal Society A: Mathematical, Physical and Engineering Sciences. 368(1919): 2369-2393.

[34] Masuda Y. Fujinaga Y, Naganaw S *et al*. (1999). Modeling and experimental studies on dissociation of methane gas hydrates in Berea sandstone cores. In Proceedings of the third International Gas Hydrate Conference. 7: 18-22. Salt Lake City, USA.

[35] Masui A, Haneda H, Ogata Y *et al*. (2006). Triaxial Compression test on submarine sediment containing methane hydrate in deep sea off the coast off Japan. InProceedings of the 41st Annual Conference, Japanese Geotechnical Society, Kagoshima, Japan.

[36] McConnell D R, Zhang Z and Boswell R. (2012). Review of progress in evaluating gas hydrate drilling hazards. Marine and Petroleum Geology. 34(1): 209-223.

[37] Milkov A V. (2004). Global estimates of hydrate-bound gas in marine sediments: how much is really out there? Earth-science Reviews. 66(3-4): 183-197.

[38] Miyazaki K, Masui A, Sakamoto Y *et al*. (2011). Triaxial compressive properties of

artificial methane-hydrate-bearing sediment. Journal of Geophysical Research: Solid Earth. 116: B6120.

[39] Miyazaki K, Tenma N, Aoki K *et al*. (2012). A nonlinear elastic model for triaxial compressive properties of artificial methane-hydrate-bearing sediment samples. Energies. 5(10): 4057-4075.

[40] Moridis G J. (2012). TOUGH+ HYDRATE v1. 2 User's manual: A code for the simulation of system behavior in hydrate-bearing geologic media. Berkeley: Lawrence Berkeley National Laboratory.

[41] Moridis G J, Queiruga A F and Reagan M T. (2019). Simulation of gas production from multilayered hydrate-bearing media with fully coupled flow, thermal, chemical and geomechanical processes using TOUGH+Millstone. Part 1: Numerical modeling of hydrates. Transport in Porous Media. 128(2): 405-430.

[42] Moridis G J, Seol Y and Kneafsey T J. (2005). Studies of reaction kinetics of methane hydrate dissociation in porous media. In Proceedings of the fifth international conference on gas hydrates. Trondheim, Norway.

[43] Nazridoust K and Ahmadi G. (2007). Computational modeling of methane hydrate dissociation in a sandstone core. Chemical engineering science. 62(22): 6155-6177.

[44] Olivella S, Gens A, Carrera J, *et al*. (1996). Numerical formulation for a simulator (CODE_BRIGHT) for the coupled analysis of saline media. Engineering Computations. 13(7): 87-112.

[45] Parente M T, Mattis S, Gupta S (2019). Efficient parameter estimation for a methane hydrate model with active subspaces. Computational Geosciences. 23(2):355-372.

[46] Philip J R and De Vries D A. (1957). Moisture movement in porous materials under temperature gradients. Eos, Transactions American Geophysical Union. 38(2): 222-232.

[47] Ruan X, Song Y C, Zhao J F *et al*. (2012). Numerical simulation of methane production from hydrates induced by different depressurizing approaches. Energies, 5(2): 438-458.

[48] Rutqvist J, Moridis G J, Grover T *et al*. (2009). Geomechanical response of permafrost-associated hydrate deposits to depressurization-induced gas production. Journal of

Petroleum Science and Engineering. 67(1-2): 1-12.

[49] Sánchez M, Santamarina J C, Teymouri M *et al*. (2018). Coupled numerical modeling of gas hydrate-bearing sediments: From laboratory to field-scale analyses. Journal of Geophysical Research: Solid Earth. 123(12): 10326-10348.

[50] Santamarina J C and Ruppel C. (2010). The impact of hydrate saturation on the mechanical, electrical, and thermal properties of hydrate-bearing sand, silts, and clay. Geophysical Characterization of Gas Hydrates, Geophys. 14: 373-384.

[51] Schrefler B A, Zhan X and Simoni L. (1995). A coupled model for water flow, airflow and heat flow in deformable porous media. International Journal of Numerical Methods for Heat and Fluid Flow. 5(6): 531-547.

[52] Selim M S and Sloan E D. (1990). Hydrate dissociation in sediment. SPE Reservoir Engineering. 5(02): 245-251.

[53] Shin H and Santamarina J C. (2017). Sediment-well interaction during depressurization. Acta Geotechnica. 12(4):883-895.

[54] Shin H and Santamarina J C. (2019). An implicit joint-continuum model for the hydro-mechanical analysis of fractured rock masses. International Journal of Rock Mechanics and Mining Sciences. 119: 140-148.

[55] Sloan E D. (2003). Fundamental principles and applications of natural gas hydrates. Nature. 426(6964): 353-359.

[56] Sloan E D and Koh C A. (2008). Clathrate hydrates of natural gases. CRC press: Boca Raton.

[57] Song B, Cheng Y, Yan C *et al*. (2019). Seafloor subsidence response and submarine slope stability evaluation in response to hydrate dissociation. Journal of Natural Gas Science and Engineering. 65: 197-211.

[58] Song Y C, Zhang L X, Lv Q *et al*. (2016). Assessment of gas production from natural gas hydrate using depressurization, thermal stimulation and combined methods. RSC Advances. 6(53): 47357-47367.

[59] Sun X, Li Y H, Liu Y *et al*. (2019). The effects of compressibility of natural gas hydrate-

bearing sediments on gas production using depressurization. Energy. 185: 837-846.

[60] Sun X, Luo H and Soga K. (2018). A coupled thermal-hydraulic-mechanical-chemical (THMC) model for methane hydrate bearing sediments using COMSOL Multiphysics. Journal of Zhejiang University-SCIENCE A. 19(8): 600-623.

[61] Sun Y, Lü X and Guo W. (2014). A review on simulation models for exploration and exploitation of natural gas hydrate. Arabian Journal of Geosciences. 7(6): 2199-2214.

[62] Teng Y H and Zhang D X. (2020). Comprehensive study and comparison of equilibrium and kinetic models in simulation of hydrate reaction in porous media. Journal of Computational Physics. 404: 109094.

[63] Teymouri M, Sánchez M and Santamarina J C. (2020). A pseudo-kinetic model to simulate phase changes in gas hydrate bearing sediments. Marine and Petroleum Geology. 120: 104519.

[64] Thomas L K, Hellums L J and Reheis G M. (1972). A nonlinear automatic history matching technique for reservoir simulation models. Society of Petroleum Engineers Journal. 12(06): 508-514.

[65] Van der Vorst Henk A. (1992). Bi-CGSTAB: A fast and smoothly converging variant of Bi-CG for the solution of nonsymmetric linear systems. SIAM Journal on scientific and Statistical Computing. 1992. 13(2): 631-644.

[66] Wang B, Fan Z, Zhao J F *et al*. (2018). Influence of intrinsic permeability of reservoir rocks on gas recovery from hydrate deposits via a combined depressurization and thermal stimulation approach. Applied Energy. 229: 858-871.

[67] Wang X R, Shao H B, Wang W Q *et al*. (2015). Numerical modeling of heating and hydration experiments on bentonite pellets. Engineering Geology. 198: 94-106.

[68] Wang Y, Feng J C, Li X S *et al*. (2016). Experimental and modeling analyses of scaling criteria for methane hydrate dissociation in sediment by depressurization. Applied Energy. 181: 299-309.

[69] Wang Y, Li X S, Li G *et al*. (2014). Experimental investigation into scaling models of methane hydrate reservoir. Applied Energy. 115: 47-56.

[70] Wang Y, Liu S, Hao F *et al*. (2017). Geothermal investigation of the thickness of gas hydrate stability zone in the north continental margin of the South China Sea. Acta Oceanologica Sinica. 36(4): 72-79.

[71] Wang Z Y, Zhang Y Y, Peng Z Y *et al*. (2022). Recent Advances in Methods of Gas Recovery from Hydrate-Bearing Sediments: A Review. Energy and Fuels. 36: 5550-5593.

[72] White M D, Kneafsey T J, Seol Y *et al*. (2020). An international code comparison study on coupled thermal, hydrologic and geomechanical processes of natural gas hydrate-bearing sediments. Marine and Petroleum Geology. 120: 104566.

[73] Wilder J W, Moridis G J, Wilson S J *et al*. (2008). An international effort to compare gas hydrate reservoir simulators. InProceedings of 6th International Conference on Gas Hydrates (ICGH 2008), Vancouver, CANADA.

[74] Wu C Y and Hsieh B Z. (2020). Comparisons of different simulated hydrate designs for Class-1 gas hydrate deposits. Journal of Natural Gas Science and Engineering. 77: 103225.

[75] Yamamoto K and Dallimore S. (2008). Aurora-JOGMEC-NRCan Mallik 2006-2008 gas hydrate research project progress. Fire in the Ice. 7 (2): 1–5.

[76] Ye J L, Qin X W, Xie W W *et al*. (2020). The second natural gas hydrate production test in the South China Sea. China Geology. 3(2): 197-209.

[77] Yin Z Y, Khurana M, Tan H K *et al*. (2018). A review of gas hydrate growth kinetic models. Chemical Engineering Journal. 342: 9-29.

[78] Yin Z, Moridis G, Tan H K *et al.* (2018). Numerical analysis of experimental studies of methane hydrate formation in a sandy porous medium. Applied Energy. 220: 681-704.

[79] Yousif M H, Abass H H, Selim M S *et al*. (1991). Experimental and theoretical investigation of methane-gas-hydrate dissociation in porous media. SPE reservoir Engineering. 6(01): 69-76.

[80] Yu T, Guan G and Abudula A. (2019). Production performance and numerical investigation of the 2017 offshore methane hydrate production test in the Nankai Trough of Japan. Applied Energy. 251: 113338.

[81] Zhao Z and Shang X. (2010). Numeric simulation for the seabed deformation in the process

of gas hydrate dissociated by depressurization. International Conference on Information Computing and Applications. (pp. 296-303). Springer, Berlin, Heidelberg.

[82] Zhou M L, Soga K and Yamamoto K. (2020). Upscaling techniques for fully coupled THM simulation and application to hydrate gas production tests. Computers and Geotechnics. 124: 103596.

[83] Zhu B, Ye Z G, Wang L J *et al*. (2020). Hydro-mechanical behavior of unsaturated soil surrounding a heated pipeline considering moisture evaporation and condensation. Computers and Geotechnics. 119: 103377.

[84] Zhu B, Ye Z G, Wang L J *et al*. (2021). Theoretical investigation into thermo-osmosis and thermofiltration effects on hydromechanical behavior of saturated soils. Journal of Engineering Mechanics. 147(4): 04021005.